JCIM JOURNAL OF CHEMICAL INFORMATION AND MODELING

pubs.acs.org/jcim Article

Promiscuous Catalytic Activity of a Binuclear *Metallohydrolase*: Peptide and Phosphoester Hydrolyses

Leonardo F. Serafim, Vindi M. Jayasinghe-Arachchige, Lukun Wang, and Rajeev Prabhakar*

Cite This: *J. Chem. Inf. Model.* 2022, 62, 2466−2480 Read Online

ACCESS | Metrics & More | Article Recommendations | Supporting Information

ABSTRACT: In this study, chemical promiscuity of a binuclear metallohydrolase *Streptomyces griseus* aminopeptidase (*Sg*AP) has been investigated using DFT calculations. *Sg*AP catalyzes two diverse reactions, peptide and phosphoester hydrolyses, using its binuclear (Zn−Zn) core. On the basis of the experimental information, mechanisms of these reactions have been investigated utilizing leucine *p*-nitro aniline (Leu-*p*NA) and bis(4-nitrophenyl) phosphate (BNPP) as the substrates. The computed barriers of 16.5 and 16.8 kcal/mol for the most plausible mechanisms proposed by the DFT calculations are in good agreement with the measured values of 13.9 and 18.3 kcal/mol for the Leu-*p*NA and BNPP hydrolyses, respectively. The former was found to occur through the transfer of two protons, while the latter with only one proton transfer. They are in line with the experimental observations. The cleavage of the peptide bond was the rate-determining process for the Leu-*p*NA hydrolysis. However, the creation of the nucleophile and its attack on the electrophile phosphorus atom was the rate-determining step for the BNPP hydrolysis. These calculations showed that the chemical nature of the substrate and its binding mode influence the nucleophilicity of the metal bound hydroxyl nucleophile. Additionally, the nucleophilicity was found to be critical for the Leu-*p*NA hydrolysis, whereas double Lewis acid activation was needed for the BNPP hydrolysis. That could be one of the reasons why peptide hydrolysis can be catalyzed by both mononuclear and binuclear metal cofactors containing hydrolases, while phosphoester hydrolysis is almost exclusively by binuclear metallohydrolases. These results will be helpful in the development of versatile catalysts for chemically distinct hydrolytic reactions.

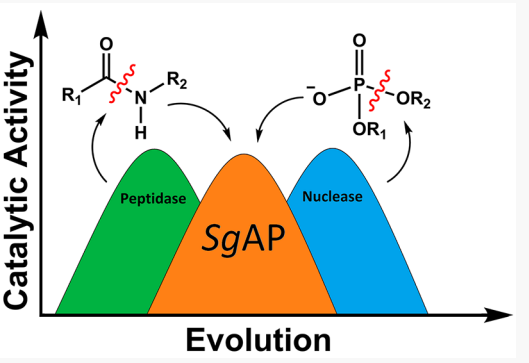

INTRODUCTION

The peptide (−(O═)C−NH−) and phosphoester ((O═)-(RO)(RO)(P−O−R)) bonds are ubiquitous in a wide range of biologically, industrially, and environmentally relevant molecules such as peptides, proteins, deoxyribonucleic acid (DNA), pharmaceuticals, pesticides, and nerve agents.[1−27] Consequently, their hydrolyses have been implicated in a wide range of critical applications like protein engineering, genomics, therapeutics, DNA repair, and remediation of pesticides and nerve agents.[28−40] However, these bonds are extremely stable, and the half-lives for the hydrolyses of peptide and phosphoester bonds are 350−600 and ∼130,000 years, respectively, at room temperature and pH 4−8.[41,42] In nature, these bonds are hydrolyzed by highly specialized mononuclear and binuclear metal center containing enzymes that depending on the nature of the scissile bond and substrate are categorized as proteases/peptidases or phosphatases/nucleases and are generally known as metallohydrolases.[5−7,15,43−57] They display significant structural diversity in terms of amino acid sequence, nature of metal ions, ligand environment, and second coordination shell residues. It is noteworthy that metalloproteases contain either a mononuclear or binuclear metal cofactor,[58,59] while metallophosphatases exclusively possess a binuclear metal cofactor.[21,60−63] Almost all members of these distinct classes of enzymes exhibit bond selectivity and perform either peptide or phosphoester hydrolysis of their substrates. One of the major factors for this selectivity is the structural similarity of the *gem*-diolate transition state formed in peptide hydrolysis with the tetrahedral phosphocenter created in the phosphoester hydrolysis. Therefore, the later motif has been commonly utilized in the design of inhibitors for proteases/peptidases.[64] However, *Streptomyces griseus* aminopeptidase (*Sg*AP) is a novel enzyme that exhibits exceptional catalytic promiscuity by hydrolyzing both peptide and phosphoester bonds with remarkable efficiency.[65,66] Although an aminopeptidase, it is capable of accelerating the first-order hydrolysis of the phosphodiester bis(4-nitrophenyl) phosphate (BNPP), commonly used model for DNA (Figure 1), by 10^{10}-fold in comparison to the uncatalyzed reaction.[65,67] This is one of the

Received: February 22, 2022
Published: April 22, 2022

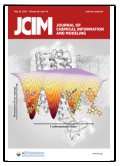

https://doi.org/10.1021/acs.jcim.2c00214
J. Chem. Inf. Model. 2022, 62, 2466−2480

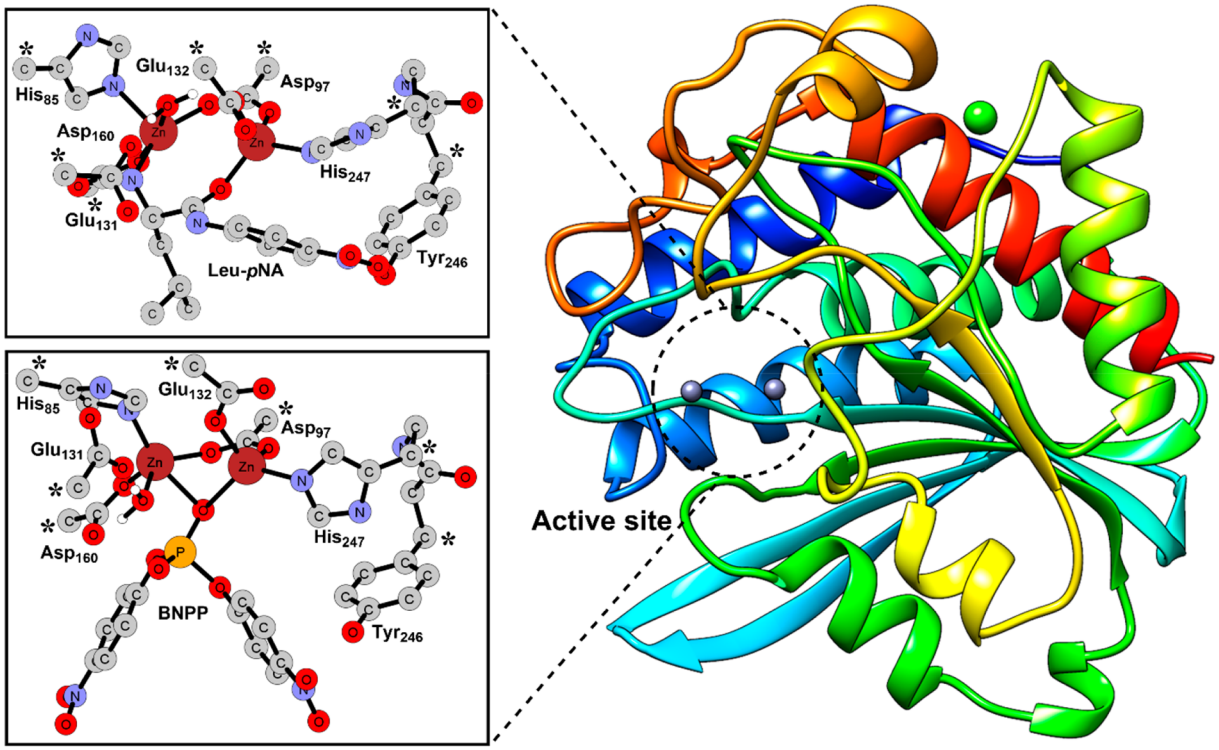

Figure 1. Leu-*p*NA and BNPP substrate-bound structures of *Sg*AP. The atoms displayed with the asterisk symbol were kept frozen in DFT calculations.

rare examples in which an aminopeptidase hydrolyzes its transition state analogue, a phosphoester, at an enormous rate. In general, members of this family cleave peptide bonds from the N-terminal of their substrates and are classified as "broad" or "narrow" depending on their substrate specificities.[68,69] Aminopeptidases such as methionine aminopeptidases (MAP)[70,71] and proline aminopeptidases (PAP) are classified as "narrow" for being able to selectively cleave peptide bonds of a specific amino acid, N-terminal Met or Pro, of the substrates. On the other hand, other peptidases such as bovine lens leucine aminopeptidase (BILAP)[72] and *Aeromonas proteolytica* aminopeptidase (AAP)[73] are classified as "broad" for being able to cleave peptides bonds formed by a wide range of hydrophobic amino acid residues of their substrates.

*Sg*AP isolated from the extracellular fluid of *S. griseus* cultures belongs to the family of "broad" range amino-peptidases.[74,75] It is a monomeric enzyme of relatively low molecular weight (30 kDa), is heat stable, and displays high and efficient catalytic turnovers. It also exhibits a preference for large hydrophobic N-terminus residues. It was the fourth aminopeptidase to have its structure determined through X-ray crystallography.[76,77] In particular, structures in the di-Zn, apo, and Hg-substituted forms of *Sg*AP have been resolved at 1.75, 2.1, and 2.1 Å resolution, respectively.[78] Additionally, cocrystal structures of *Sg*AP with methionine, leucine, and phenylalanine residues, all weak inhibitors of the enzyme, are available at 1.53, 1.70, and 1.80 Å resolution, respectively.[79,80] In the catalytically active binuclear core of the enzyme, two Zn^{2+} ions are separated by 3.6 Å. In these metal centers, each Zn^{2+} ion is coordinated to one imidazole group (Zn_1 to His_{85} and Zn_2 to His_{247}) and one carboxylate group (Zn_1 to Asp_{160} and Zn_2 to Glu_{132}) (Figure 1). Additionally, one carboxylate group (Asp_{97}) bridges both metal ions.

The general acid−base mechanisms of peptide and phosphoester hydrolyses are quite different from each other (Scheme 1a). A mechanism for peptide hydrolysis by *Sg*AP was proposed using a plethora of experimental techniques such as X-ray crystallography, site-directed mutagenesis, solvent isotope effects, pH profiling, and enzymatic inhibition and molecular dynamics (MD) simulations.[66,67,81−83] On the basis of fluoride binding experiments, a noncompetitive inhibitor of *Sg*AP under different pH conditions (5.9−8.0), the water/hydroxide molecule, was proposed to bind to both metal ions in a bridging fashion.[83] However, the fluoride ion was also reported to act as an uncompetitive inhibitor which suggested a terminal binding of the water/hydroxide molecule to a single metal ion.[84] According to the proposed mechanism, in the reactant (I), the carbonyl group of the substrate coordinates to the Zn_2 site and increases the coordination number of the metal ion to 5. The interactions of the substrate with Zn_2 and Tyr_{246} enhance the electrophilicity of its carbonyl carbon atom. In the first step, the Glu_{131} functions as a base and creates the Zn_1 bound hydroxyl nucleophile (II). In the next step, this nucleophile attacks the electrophilic carbon atom of the substrate and creates a tetrahedral *gem*-diolate intermediate (III). This intermediate is stabilized by the Zn_2 ion and Tyr_{246}. In the last step, a proton transfer from Glu_{131} to the N-terminal amine group of the substrate collapses this intermediate which separates the amine and the carboxylic acid (IV). The roles of Glu_{131} and Tyr_{246} in the mechanism were suggested by site-directed mutagenesis experiments.[81] The Glu_{131}Ala mutation caused approximately a 4 to 5 orders of magnitude decrease in k_{cat} but did not significantly affect K_m, which supported its role as a general base. On the other hand, the Tyr_{246}(Ser, Ala, or Phe) mutations resulted in about a 100-fold reduction of

https://doi.org/10.1021/acs.jcim.2c00214
J. Chem. Inf. Model. 2022, 62, 2466−2480

Scheme 1. General Acid−Base Mechanism of Peptide (a) and Phosphoester (b) Hydrolyses

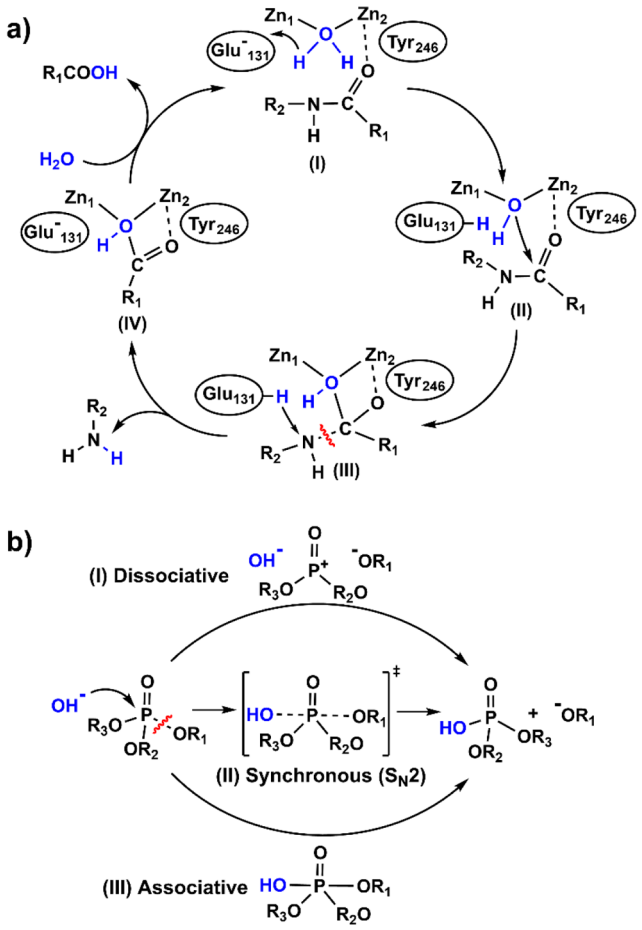

activity that suggested its involvement in stabilization of the enzyme−substrate complex.

In contrast to the aforementioned experimental information available for the peptide hydrolysis, very little is known about the mechanism of phosphoester hydrolysis catalyzed by *Sg*AP. In general, this reaction has been proposed to occur through three distinct mechanisms shown in the More O'Ferrall−Jencks diagram (Scheme 1b):[85] (I) Dissociative or elimination−addition mechanism: This proceeds via a trigonal metaphosphate intermediate, and the release of the leaving group (R_1O) precedes the formation of a bond between the phosphate and nucleophile (OH^-−P^+). (II) Dissociative associative or synchronous mechanism: This S_N2 type mechanism proceeds through the simultaneous formation and cleavage of the phosphoester bonds. (III) Associative or addition−elimination mechanism: This mechanism takes place via a pentavalent phosphorane intermediate formed by the attacking nucleophile. It has been observed that phosphodiester hydrolysis occurs through either the synchronous or associative mechanisms, and a fully dissociative mechanism has not yet been observed.[75,86] In general, binuclear metallohydrolases have been reported to utilize one of these mechanisms depending on the chemical nature of the substrate.[15,54,75,86−100]

The thermostability of *Sg*AP allowed the determination of the rate of the reaction at a wide range of temperature (20−60 °C) for multiple substrates.[66,67,83] The kinetic and thermodynamic parameters for the hydrolysis of different amino acid (Gly, Met, Val, Ala, Lys)−*p*NA (para-nitro aniline) analogues and BNPP by *Sg*AP were measured.[66] Among them, Leu-*p*NA was found to be the fastest substrate for this enzyme (k_{cat} = 657 ± 54 s^{-1}, $\Delta G^{\ddagger}$ = 13.9 ± 0.1 kcal/mol). However, *Sg*AP also exhibited a significant activity toward BNPP hydrolysis (k_{cat} = 0.42 ± 0.01 s^{-1}, $\Delta G^{\ddagger}$ = 18.3 kcal/mol). On the basis of the measured thermodynamic parameters, it was suggested that the hydrolyses of peptides and BNPP involve similar chemical interactions at the rate-determining step. However, proton transfer steps are different in these reactions. Peptide hydrolysis involves necessarily at least two-proton transfer steps, while BNPP hydrolysis may involve only one. The solvent isotope effect experiments[83] also confirmed two-proton transfer steps in Leu-*p*NA hydrolysis at pH 6.5. It was concluded that the rate-determining step is pH dependent. The deprotonation of the Zn-bound water molecule exerts a greater effect on the reaction rate than the protonation of the peptide bond nitrogen by Glu_{131} at pH 6.5, while at pH > 8 the collapse of the *gem*-diolate intermediate becomes the rate-determining step in a single-proton transfer process.

Despite the availability of the aforementioned experimental information, there remain the following outstanding questions regarding the functioning of this interesting enzyme. What are the binding modes of peptide and phosphoester substrates? Does the water/hydroxyl nucleophile coordinate in either a bridging or terminal fashion to the binuclear core? Which metal site (Zn_1 or Zn_2) is the most suitable to generate the hydroxyl nucleophile from a water molecule? What is the exact mechanism for phosphoester hydrolysis? What are the effects of Lewis acid and nucleophile activation in these reactions? In this study, all these questions have been addressed using DFT calculations. They will also elucidate why peptide hydrolysis can be catalyzed by both mononuclear and binuclear cofactors containing metallohydrolases, while phosphoester hydrolysis can be catalyzed by only binuclear metallohydrolases. The results gleaned from these calculations will provide deeper insights into the unique chemical promiscuity exhibited by *Sg*AP which may also be relevant to other metalloenzymes. They will help us derive guiding principles for the rational design of versatile catalysts for diverse hydrolytic reactions.

COMPUTATIONAL DETAILS

Computational Modeling. The model of the enzyme active site was built from the available high resolution (1.75 Å) X-ray structure (PDB ID: 1XJO).[74] Among all the X-ray structures available for this enzyme, it contained the natural binuclear Zn−Zn metal core and a phosphate analogue of the substrate. The Leu-*p*NA dipeptide and BNPP phosphodiester were used as the substrates. Their charges and electrostatic potentials (ESP) were computed at the B3LYP/6-311G+(d,p) level of theory using Gaussian 16 software.[101] The force field parameters of both substrates were then developed using antechamber, an in-built tool in the AMBER software package.[102] The enzyme−substrate models were built through molecular docking using AutoDock Vina 1.5.6 software.[103] In the rigid docking protocol used here, the structure of the enzyme was kept fixed, but the substrates were allowed to adopt any conformations. This procedure provided 20 poses each for both substrates. They were ranked on the basis of their energies. The three poses with the lowest energies for each substrate were selected for the further energy minimizations. They were subsequently solvated in a cubic

https://doi.org/10.1021/acs.jcim.2c00214
J. Chem. Inf. Model. 2022, 62, 2466−2480

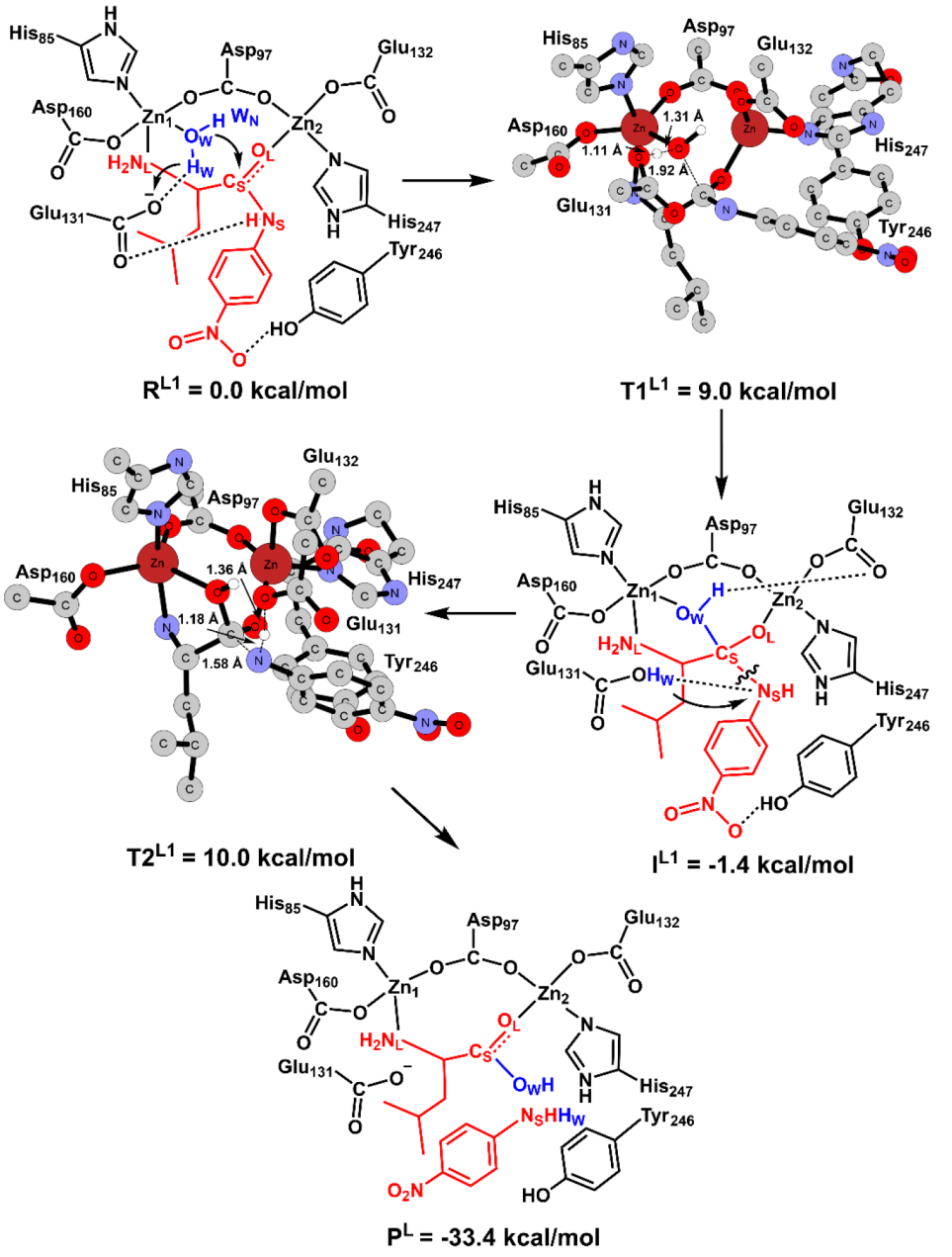

Figure 2. Mechanism of the Leu-*p*NA hydrolysis in the $M1^L$ pathway.

10 nm × 10 nm × 10 nm box using the TIP3P water molecules.[104−106] The shortest distance from the surface of the protein to the edge of the box was 1.0 nm. The total charge of the system was neutralized by the addition of Na^+ and Cl^- ions to mimic the physiological concentration (0.154 M). Electrostatic interactions were calculated using the particle mesh Ewald method, and a cutoff of 1.2 nm was set for both van der Waals and Coulombic interactions. Energy minimization of the initial structures were performed for 3000 steps using the steepest descent algorithm.

The equilibrated structures of the enzyme−substrate complexes were then used to build the truncated models for the DFT calculations. They include both metal ions (Zn_1 and Zn_2) and all the first coordination shell residues bound to Zn_1 (Asp_{97}, Glu_{132}, and His_{247}) and Zn_2 (His_{85}, Asp_{97}, and Asp_{160}) (Figure 1). The Asp_{97} residue bridges both metals and keep their coordination number to 4 in the absence of the substrate and the nucleophile. The second coordination shell residues (Glu_{131} and Tyr_{246}) relevant to the catalytic mechanisms were also incorporated in the model. There are four charged Glu/Asp residues in this model. Among them, three (Asp_{27}, Asp_{160} ,and Glu_{132}) coordinate directly with the binuclear metal center. The fourth (Glu_{131} base) formed hydrogen bonds with the metal bound water and substrate. Therefore, the effect of the neighboring residues around charged catalytic residues in this enzyme is expected to be small and not likely to influence the computed energetics. On the basis of these considerations, this model should be adequate to investigate the mechanism of this reaction.[107,108]

To retain the steric effect of the surrounding protein in the active site, the carbon atom leading to the backbone of these residues was constrained in its position from the equilibrated structure (Figure 1). Therefore, Asp_{97}, Glu_{131}, Glu_{132}, and Asp_{160} were treated as acetate ions, while His_{85} was treated as

https://doi.org/10.1021/acs.jcim.2c00214
J. Chem. Inf. Model. 2022, 62, 2466−2480

5-methylimidazole. The backbones of the second coordination shell (Tyr_{246} and His_{247} residues) were included in the model. The overall charges of the models used for Leu-*p*NA and BNPP hydrolyses were 0 and −1, respectively and they all existed in the singlet spin state.

Computational Procedure. The geometries of all structures were optimized using the Gaussian 16 software package using the MPW1PW91 functional.[109] The 6-31G+(d) basis set was used for all atoms except P and Zn. The P atom was treated using the 6-311G(d,p) basis set and Zn utilizing the Lanl2dz basis set with the corresponding Hay−Wadt effective core potential.[110−115] The dispersion effects were included using the Grimme's function with the Becke−Johnson damping effect (GD3BJ).[116] The energies of the optimized structures were improved by performing single point calculations using the Lanl2tz basis set for Zn and the 6-311G+(d,p) basis set of triple-ζ quality for the remaining atoms. The solvation effects were included using the polarizable continuum model (IEFPCM).[117,118] In these calculations, diethyl ether (ε = 4.3) was used to incorporate the hydrophobic environment of the protein active site. Hessians were calculated at the same level of theory as the optimizations to confirm the nature of the stationary points along the reaction coordinate. The transition states were confirmed to have only one imaginary frequency corresponding to the reaction coordinates. Thermal, entropy, and zero-point vibrational corrections were added to the final energies at 298 K and 1 atm that included corrections due to frozen atoms. The energetically most feasible mechanism for each substrate was also investigated using the B3LYP[119] and M06-2X[120] functionals, and the barrier differences between these functionals were found to be less than 1.0 kcal/mol. These small energy differences showed that computed energies for this system were not sensitive to the level of theory used in these calculations.

RESULTS AND DISCUSSION

Enzyme−Substrate Interactions and Location of the Nucleophile. The Leu-*p*NA and BNPP substrates can bind in different modes to the binuclear metal core of *Sg*AP. Additionally, the nucleophile-generating water molecule (W_N) can coordinate either terminally to Zn_1 or Zn_2 or in a bridging (μ-W_N) manner to both metal ions. All these different modes of the substrate and nucleophile binding created 12 distinct conformations for each substrate. Their structures and relative energies (in gas phase) for Leu-*p*NA and BNPP are shown in Figures S1 and S2, respectively.

Both functional groups (carbonyl and amine) of Leu-*p*NA can interact with the binuclear metal core. In the lowest energy conformation ($\mathbf{R^{L2}}$ in Figure S1) for this substrate, the amine group coordinates to Zn_1, while the carbonyl group to Zn_2. In $\mathbf{R^{L2}}$, the W_N water is bound to Zn_2. The switching of W_N from Zn_2 to Zn_1, while retaining the conformation of Leu-*p*NA generates another structure ($\mathbf{R^{L1}}$) that is 4.0 kcal/mol higher in energy. The conformation ($\mathbf{R^{L3}}$) with a bridging water (μ-W_N) is even higher, i.e., 7.3 kcal/mol in comparison to $\mathbf{R^{L2}}$. As shown in Figure S1, all other conformations are much higher in energy, and in many of them, the substrate loses its coordination to one of the metal sites.

For the BNPP substrate, one phosphate oxygen atom of BNPP bridges both Zn ions in the lowest energy conformation ($\mathbf{R^{B1}}$ in Figure S2). In $\mathbf{R^{B1}}$, the W_N water is coordinated to Zn_1. This binding mode for BNPP resembles L-tryptophan and *p*-iodo-L-phenylalanine inhibitors of *Sg*AP.[82] The switching of W_N to Zn_2 in $\mathbf{R^{B1}}$ creates another structure ($\mathbf{R^{B2}}$) that is only 2.2 kcal/mol higher in energy from $\mathbf{R^{B1}}$. The bridging μ-H_2O conformation for this substrate is significantly higher (13.8 kcal/mol) in energy than $\mathbf{R^{B1}}$. All other structures in which BNPP is bound to either Zn_1 or Zn_2 with terminally coordinated W_N are much higher in energy than $\mathbf{R^{B1}}$ (Figure S2).

In this study, due to small energy differences and structural properties, the three ($\mathbf{R^{L2}}$, $\mathbf{R^{L1}}$, and $\mathbf{R^{L3}}$) lowest and distinct conformations for Leu-*p*NA (Figures S1) and two ($\mathbf{R^{B1}}$ and $\mathbf{R^{B2}}$) for BNPP (Figure S2) are used to investigate their hydrolysis. Since the nature of the nucleophile (H_2O or −OH) is not known, an additional structure with the bridging hydroxyl group is also utilized for both substrates.

Peptide (Leu-*p*NA) Hydrolysis. Since Leu-*p*NA has been reported as the fastest substrate of *Sg*AP,[66] it is used to study peptide hydrolysis. Depending on the binding site and nature of the nucleophile (H_2O or OH), the Leu-*p*NA hydrolysis can occur through the four potential ($M1^L$, $M2^L$, $M12^L$, and $M12^{LOH}$) pathways discussed below.

$M1^L$ Pathway. In the reactant ($\mathbf{R^{L1}}$) of this pathway, the Leu-*p*NA substrate interacts with Zn_1 and Zn_2 through its amine and carbonyl groups, respectively, and W_N water (HO_WH_W) is coordinated only to Zn_1 (Zn_1−O_W = 2.16 Å, Zn_1−N_L = 2.15 Å, Zn_2−O_L = 2.00 Å, and Zn_1−Zn_2 = 3.82 Å in Figure 2 and Table 1). In this binding mode, the carbonyl bond (C_S−O_L) of Leu-*p*NA elongates by 0.04 Å, and consequently, the scissile peptide (C_S−N_S) bond shrinks by 0.03 Å in comparison to the corresponding bond in its free form. These changes suggest the absence of Lewis acid activation of the peptide bond in this structure. On the other hand, Zn_1 bound W_N becomes more acidic; i.e., its O_W−H_W bond length increases to 1.02 Å. Metallohydrolases are generally known to drastically decrease the ionization constant of the metal-coordinated water by greater than 10^8-fold, i.e., pK_a = 14 to ∼7.[121,122] The pK_a of 6 obtained by kinetic measurements correlates well with a terminal Zn-bound water in *Sg*AP[66] and other Zn-containing hydrolases.[123,124] This substrate binding mode is also stabilized by a hydrogen bond with Tyr_{246}. In the first step of this mechanism, as proposed experimentally,[81] Glu_{131} acts as a general base and generates the nucleophile (O_WH) from W_N through an abstraction of its H_w proton. This process occurs concomitantly with the nucleophilic attack by the −O_WH group to the electrophilic carbon atom (C_s) of the scissile peptide bond to form the *gem*-diolate intermediate ($\mathbf{I^{L1}}$ in Figure 2). From $\mathbf{R^{L1}}$, this concerted step takes place with a barrier of 9.0 kcal/mol through transition state ($\mathbf{T1^{L1}}$ in Figure 2). The $\mathbf{I^{L1}}$ intermediate formed in this process is slightly exergonic (1.4 kcal/mol), and in this structure, the nucleophile is attached to both Zn_1 and C_s to form a five-membered ring. The sum of the internal angles of this ring in $\mathbf{I^{L1}}$ is 493°. As suggested by the site-directed mutagenesis experiments,[81] this intermediate is stabilized through a hydrogen bond by Tyr_{246}. In comparison to $\mathbf{R^{L1}}$, the Zn_1−Zn_2 distance becomes shorter by 0.07 Å, and the scissile C_S−N_S bond in $\mathbf{I^{L1}}$ is significantly activated by 0.11 Å (C_S−N_S = 1.46 Å, Table 1). In the next step, Glu_{131} switches its function to an acid and donates its previously acquired proton (H_w) to the N_s atom to cleave the scissile C_S−N_S bond. This process takes place with a barrier of 11.4 kcal/mol from $\mathbf{I^L}$. As proposed experimentally, the Leu-*p*NA hydrolysis is found to take place through a two-proton transfer process.[66,83]

https://doi.org/10.1021/acs.jcim.2c00214
J. Chem. Inf. Model. 2022, 62, 2466−2480

Table 1. Key Bond Distances (in Å) in Reactants, Transition States, Intermediates, and Products in Leu-*p*NA Hydrolysis

$M1^L$	$\mathbf{R}^{L1}$	$\mathbf{T1}^{L1}$	$\mathbf{I}^{L1}$	$\mathbf{T2}^{L1}$	$\mathbf{P}^L$	–	–
Zn_1–Zn_2	3.82	3.70	3.75	3.51	3.96	–	–
Zn_1–O_W	2.16	2.14	2.57	2.31	4.40	–	–
Zn_2–O_W	3.27	2.92	3.06	2.71	3.31	–	–
O_W-H_W	1.02	1.31	1.45	2.35	6.24	–	–
Glu_{131}–H_W	1.63	1.11	1.05	1.36	1.64	–	–
Zn_1–N_L	2.15	2.18	2.12	2.12	2.12	–	–
Zn_2–O_L	2.00	1.98	1.94	1.97	2.00	–	–
O_W-C_S	3.50	1.92	1.50	1.48	1.30	–	–
C_S–N_S	1.35	1.41	1.46	1.58	6.84	–	–
$M2^L$	$\mathbf{R}^{L2}$	$\mathbf{T1}^{L2}$	$\mathbf{I}^{L2}$	$\mathbf{T2}^{L2}$	$\mathbf{P}^L$	–	–
Zn_1–Zn_2	3.90	3.79	3.73	3.73	3.96	–	–
Zn_1–O_W	4.84	4.11	4.20	3.84	3.31	–	–
Zn_2–O_W	2.21	2.18	3.13	2.23	4.40	–	–
O_W–H_W	1.02	1.39	1.50	2.34	6.24	–	–
Glu_{131}–H_W	1.62	1.11	1.06	1.43	1.64	–	–
Zn_1–N_L	2.10	2.09	2.10	2.10	2.12	–	–
Zn_2–O_L	2.15	2.13	2.03	2.10	2.00	–	–
O_W–C_S	2.93	1.91	1.56	1.44	1.30	–	–
C_S–N_S	1.36	1.41	1.46	1.76	6.84	–	–
$M12^L$	$\mathbf{R}^{L3}$	$\mathbf{T1}^{L3}$	$\mathbf{I}^{L3}$	$\mathbf{T2}^{L3}$	$\mathbf{P}^L$	–	–
Zn_1–Zn_2	3.69	3.91	3.67	3.91	3.96	–	–
Zn_1–O_W	2.19	2.11	2.16	2.15	4.40	–	–
Zn_2–O_W	2.20	3.15	3.00	2.90	3.31	–	–
O_W–H_W	1.05	1.25	3.35	2.49	6.24	–	–
Glu_{131}–H_W	1.44	1.15	1.10	1.58	1.64	–	–
Zn_1–N_L	2.17	2.20	2.20	2.15	2.12	–	–
Zn_2–O_L	2.12	1.95	1.94	1.94	2.00	–	–
O_W–C_S	2.86	1.90	1.48	1.45	1.30	–	–
C_S–N_S	1.34	1.39	1.46	1.59	6.84	–	–
$M12^{LOH}$	$\mathbf{R}^{LOH}$	$\mathbf{T1}^{LOH}$	$\mathbf{I1}^{LOH}$	$\mathbf{T2}^{LOH}$	$\mathbf{I2}^{LOH}$	$\mathbf{T3}^{LOH}$	$\mathbf{P}^{LOH}$
Zn_1–Zn_2	3.46	3.55	3.59	3.62	3.54	3.52	3.55
Zn_1–O_W	1.99	2.12	2.38	2.23	2.00	2.00	2.19
Zn_2–O_W	1.91	1.97	2.12	2.15	2.00	2.00	1.98
Glu_{131}–H_W	2.00	1.71	1.43	1.40	1.39	1.23	1.78
Zn_1–N_L	2.32	2.22	2.21	2.21	2.23	2.24	2.19
Zn_2–O_L	5.05	2.44	2.09	2.07	2.17	2.16	3.10
O_W–C_S	3.35	1.89	1.52	1.51	1.41	1.42	1.32
C_S–N_S	1.38	1.44	1.49	1.49	1.53	1.65	3.40

In the transition state ($\mathbf{T2}^{L1}$ in Figure 2) for this concerted step, the C_S–N_S distance is the longest (1.58 Å), and the Zn_1–Zn_2 distance is the shortest (3.51 Å) among all structures (Table 1). This step is slightly more favored to be the rate-limiting step of the mechanism. On the basis of solvent KIEs also, creation of the nucleophile in the first step and collapse of the *gem*-diolate intermediate in the second step have been proposed to be rate-determining steps at pH = 6.5 and <8, respectively. In the final product ($\mathbf{P}^L$), the nitroaniline fragment is completely separated from the substrate, but the leucine fragment is still bound to both metal ions. $\mathbf{P}^L$ is 33.4 kcal/mol exergonic from $\mathbf{R}^{L1}$.

These calculations suggest that in the absence of Lewis acid activation of the substrate by the metal center the nucleophilicity of the hydroxyl ion plays a critical role in the reaction. The second step associated with the cleavage of the peptide bond is likely to be the rate-limiting step of the mechanism.

$M2^L$ Pathway. In the reactant ($\mathbf{R}^{L2}$ in Figure S3) of this pathway, the W_N water is coordinated to the Zn_2 site of the binuclear metal core. In $\mathbf{R}^{L2}$, the Leu-*p*NA substrate is coordinated in the same overall orientation as in $\mathbf{R}^{L1}$; i.e., the amine and carbonyl group interact with Zn_1 and Zn_2, respectively. However, the Zn_1–Zn_2 distance of 3.90 Å in $\mathbf{R}^{L2}$ is 0.08 Å longer than the one in $\mathbf{R}^{L1}$ (Table 1). The Zn_1–N_L and Zn_2–O_L bond distances in $\mathbf{R}^{L2}$ are 0.05 and 0.15 Å shorter and longer, respectively, than the corresponding distances in $\mathbf{R}^{L1}$ (Table 1). The W_N water is less tightly coordinated to Zn_2, and the Zn_2–W_N distance of 2.21 Å is 0.05 Å longer than the corresponding distance in $\mathbf{R}^{L1}$. The same length (1.02 Å) of the O_W–H_W bond of W_N in both reactants shows that both nearly identical metal sites exert the same influence on its acidity (Table 1). The scissile peptide bond C_S–N_S (1.36 Å) of Leu-*p*NA is also shortened by 0.02 Å in $\mathbf{R}^{L2}$, albeit slightly less (by 0.01 Å) than this bond in $\mathbf{R}^{L1}$. From $\mathbf{R}^{L2}$, formation of the *gem*-diolate intermediate ($\mathbf{I}^{L2}$) through proton abstraction by Glu_{131} base occurs with a barrier of 14.4 kcal/mol. It is 5.4 kcal/mol higher than the corresponding barrier in the $M1^L$ pathway. The higher barrier in the $M2^L$ pathway is caused by the creation of a more strained four-membered ring transition state ($\mathbf{T1}^{L2}$) and a longer W_N–Glu_{131} (nucleophile–electrophile) distance. Although Glu_{131} is quite flexible to create the hydroxyl nucleophile on both metal sites, it is located about 1.0 Å closer to Zn_1 than to Zn_2. Furthermore, $\mathbf{I}^{L2}$ is 6.4 kcal/mol endergonic from $\mathbf{R}^{L2}$, while $\mathbf{I}^{L1}$ is slightly (1.4 kcal/mol) more exergonic from $\mathbf{R}^{L1}$. In $\mathbf{I}^{L2}$, the $-O_WH_W$ group loses its interaction with Zn_2 and completely transfers to the C_s atom of the substrate. It also lacks extra stabilization provided by hydrogen bonding with Glu_{131} and Glu_{132}. However, the lengths of the scissile C_S–N_S bonds in both $\mathbf{I}^{L2}$ and $\mathbf{I}^{L1}$ are exactly the same (C_S–N_S = 1.46 Å). The collapse of the *gem*-diolate intermediate through the transition state ($\mathbf{T2}^{L2}$) occurs with a barrier of 17.8 kcal/mol from $\mathbf{R}^{L2}$. This process takes exactly the same barrier (11.4 kcal/mol) in both $M1^L$ and $M2^L$ pathways. Since this process follows a step that was endergonic by 6.4 kcal/mol in this pathway, the overall barrier becomes 17.8 kcal/mol from $\mathbf{R}^{L2}$.

These results suggest that the preferential coordination of the nucleophile-generating W_N water to either the Zn_1 or Zn_2 site affects only the first step of the mechanism. Since $\mathbf{R}^{L2}$ is computed to be 2.8 kcal/mol exergonic than $\mathbf{R}^{L1}$, the reaction can start from the former. $\mathbf{R}^{L2}$ then transforms into $\mathbf{R}^{L1}$, and the subsequent reaction proceeds through the $M1^L$ pathway discussed above. The overall barrier of the 14.2 kcal/mol for such a pathway will be 3.6 kcal/mol lower than the $M2^L$ pathway (Figure S3).

$M12^L$ Pathway. Since the exact binding mode (terminal or bridging) of the nucleophile-generating W_N water is a matter of debate,[66,82,83] another pathway ($M12^L$) starting from its bridging form is also explored (Figure S4). In the reactant ($\mathbf{R}^{L3}$) of this pathway, W_N is symmetrically bound to both Zn ions (Zn_1–O_W = 2.19 Å and Zn_2–O_W = 2.20 Å in Table 1). It also forms two strong hydrogen bonds with Glu_{131} and Glu_{132}. This binding mode and a strong polarization by Glu_{131} lead to a much greater activation of W_N in comparison to both $\mathbf{R}^{L1}$ and $\mathbf{R}^{L2}$ (O_W–H_W = 1.05 Å, Table 1). However, the scissile peptide bond C_S–N_S of 1.34 Å in $\mathbf{R}^{L3}$ is the strongest among all three reactants. Additionally, the Zn_1–Zn_2 distance of 3.69 Å (Table 1) in this structure is also the shortest among all three reactants. It weakens the interaction of the substrate with the metal center (Zn_1–N_L = 2.17 Å and Zn_2–O_L = 2.12 Å in Table 1). Despite a weaker O_W–H_W bond, the barrier of 17.0 kcal/mol for the proton transfer to the Glu_{131} base and

https://doi.org/10.1021/acs.jcim.2c00214
J. Chem. Inf. Model. 2022, 62, 2466–2480

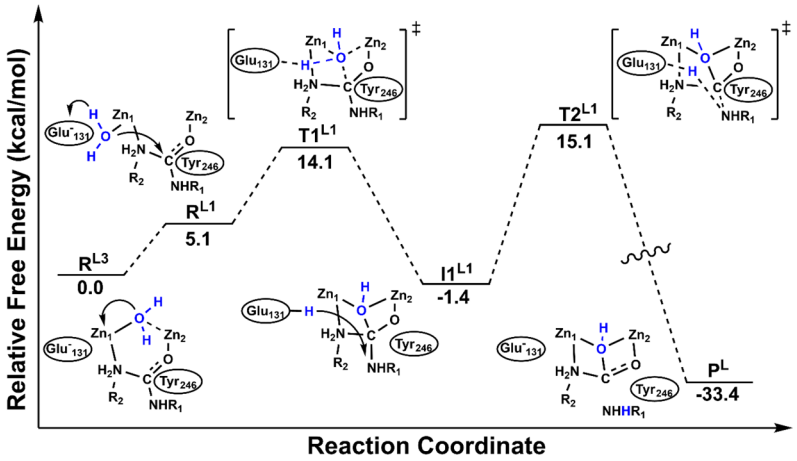

Figure 3. Most plausible mechanism for the Leu-*p*NA hydrolysis by *Sg*AP. The arrows describe the transfer of atoms.

synchronous nucleophilic attack is the highest among all three pathways. This could be due to a weak nucleophilicity of the $-O_WH_W$ group caused by its interaction with both metal ions in $\mathbf{R}^{L3}$. However, in the transition state ($\mathbf{T1}^{L3}$ in Figure S4) for this step, the nucleophile is delivered by only the Zn_1 site (Table 1). Additionally, the intermediate ($\mathbf{I}^{L3}$) form in this step is the most unstable, i.e., 10.7 kcal/mol endergonic from $\mathbf{R}^{L3}$. In the next step, the collapse of $\mathbf{I}^{L3}$ through proton donation by Glu_{131} occurs with an overall barrier of 18.8 kcal/mol. The formation of $\mathbf{I}^{L3}$, similar to $\mathbf{I}^{L2}$ in the $M2^L$ pathway, is endergonic by 10.7 kcal/mol. It also lacks the stabilization provided by Tyr_{246} and possesses much longer $Glu_{131}-H_w$ bond (1.10 Å in Table 1). Due to its relatively higher energy, the collapse of $\mathbf{I}^{L3}$ through $\mathbf{T2}^{L3}$ takes place with a barrier of 8.1 kcal/mol. However, the oval barrier for this process becomes 18.8 kcal/mol from $\mathbf{R}^{L3}$. Since this pathway proceeds with the highest barrier computed in all three pathways, it can be ruled out.

Since $\mathbf{R}^{L3}$ is the most stable reactant (2.3 and 5.1 kcal/mol exergonic than $\mathbf{R}^{L2}$ and $\mathbf{R}^{L1}$, respectively), it is most likely to be starting point of the reaction. The thermodynamic stability of this structure is also supported by the fluoride inhibition experiments.[83] $\mathbf{R}^{L3}$ can transform into $\mathbf{R}^{L1}$ and the subsequent reaction occurs through the $M1^L$ pathway (Figure 3). The overall barrier of 16.5 kcal/mol for such a pathway ($M12^{L1}$) is in good agreement with the measured value of 13.9 kcal/mol.[66] This barrier is also 2.7 kcal/mol lower than the previous pathway that starts from $\mathbf{R}^{L2}$ and continues through $\mathbf{R}^{L2} \rightarrow \mathbf{R}^{L1}$ transformation. This mechanism will address the unresolved issue in the literature regarding the terminal or bridging binding mode of water molecule to the metal center of *Sg*AP.

$M12^{LOH}$ Pathway. Since the protonation state (H_2O or $-OH$) of the bridging W_N is not known, its bridging hydroxyl (μ-O_WH_W) form is also explored in the $M12^{LOH}$ pathway (Figure S5). This form of nucleophile has also been proposed to be utilized by other binuclear metallohydrolases such as BILAP[125] and AAP.[126] In the reactant ($\mathbf{R}^{LOH}$) of this pathway, the carbonyl group of the substrate loses its interaction with the Zn_2 ion, and the scissile C_S-N_S bond length (1.38 Å) remains unchanged from its free form (Figure S5, Table 1). It is noteworthy that this bond became stronger in $\mathbf{R}^{L1}$, $\mathbf{R}^{L2}$, and $\mathbf{R}^{L3}$ (Table 1) after the binding of the substrate to the metal ion. Additionally, in this binding mode, the Zn_1-Zn_2 distance is much shorter (3.46 Å) than the previous reactants (Table 1).

In $\mathbf{R}^{LOH}$, the bridging hydroxyl (μ-O_WH_W) is coordinated in an asymmetric manner, and its interaction with the Zn_2 ion is stronger than the one with the Zn_1 ion (Zn_1-O_W = 1.99 Å and Zn_2-O_W = 1.91 Å, Table 1). In the first step of the mechanism, the μ-O_WH_W group attacks the C_S atom of the substrate to form the *gem*-diolate intermediate ($\mathbf{I1}^{LOH}$ in Figure S5). However, in the transition state ($\mathbf{T1}^{LOH}$), the nucleophile is delivered by only the Zn_2 site (Zn_2-O_W = 1.91 Å in Table 1), and the Zn_1-O_W distance is much longer (2.12 Å). This step occurs with a barrier of 14.9 kcal/mol. The intermediate ($\mathbf{I1}^{LOH}$) formed in this step is highly endergonic by 14.0 kcal/mol. In $\mathbf{I1}^{LOH}$, O_W is coordinated to Zn_2 and C_s atoms to form a $\mathbf{I}^{L3}$-like four-member ring. In this intermediate, the $-O_WH_W$ group is coordinated only to the Zn_2 ion (Zn_2-O_W = 2.12 Å), and the C_S-N_S peptide bond is more activated (1.49 Å) than the corresponding bond in $\mathbf{I}^{L1}$, $\mathbf{I}^{L2}$ and $\mathbf{I}^{L3}$. Since Glu_{131} in $\mathbf{I1}^{LOH}$ remains charged in comparison to its neutral form in the $M1^L$, $M2^L$, and $M12^L$ pathways, this pathway requires an additional step. In $\mathbf{I1}^{LOH}$, the H_w proton is quite distant (2.5 Å) to be transferred directly to the N_s atom of the scissile bond. In the next step, Glu_{131} acts as a base and abstracts the H_w proton with a small barrier of 4.5 kcal/mol from $\mathbf{I}^{LOH}$, i.e., 18.5 kcal/mol from $\mathbf{R}^{LOH}$. The intermediate ($\mathbf{I2}^{LOH}$) formed through the transition state ($\mathbf{T2}^{LOH}$) is endergonic by 17.3 kcal/mol (Figure S5). In $\mathbf{I2}^{LOH}$, the peptide bond is significantly activated (C_S-N_S = 1.53 Å) and ready to be cleaved. In the next step, Glu_{131} donates its previously acquired H_w proton to the N_s atom and cleaves the C_S-N_S bond with a low barrier of 2.2 kcal/mol from $\mathbf{I2}^{LOH}$. Since this step is followed by a step that was endergonic by 17.3 kcal/mol, the overall barrier for the step becomes 19.5 kcal/mol from $\mathbf{R}^{LOH}$. It is the rate-limiting step of the entire mechanism. The rate-limiting barrier for this pathway is found to be 4.4 kcal/mol higher than the most feasible mechanism shown in Figure 3.

The computed energetics suggest that this pathway requires an additional step and is energetically least favorable among all other pathways. Therefore, it can be ruled out.

Phosphoester (BNPP) Hydrolysis. Similar to Leu-*p*NA, BNPP hydrolysis can also occur through three different $M1^B$, $M2^B$, and $M12^{BOH}$ pathways. Since the bridging μ-H_2O bound reactant is much higher (10.4 kcal/mol in Figure S2) in energy than the most stable reactant ($\mathbf{R}^{B2}$ in Figure S2), a pathway starting from this structure is not explored.

https://doi.org/10.1021/acs.jcim.2c00214
J. Chem. Inf. Model. 2022, 62, 2466−2480

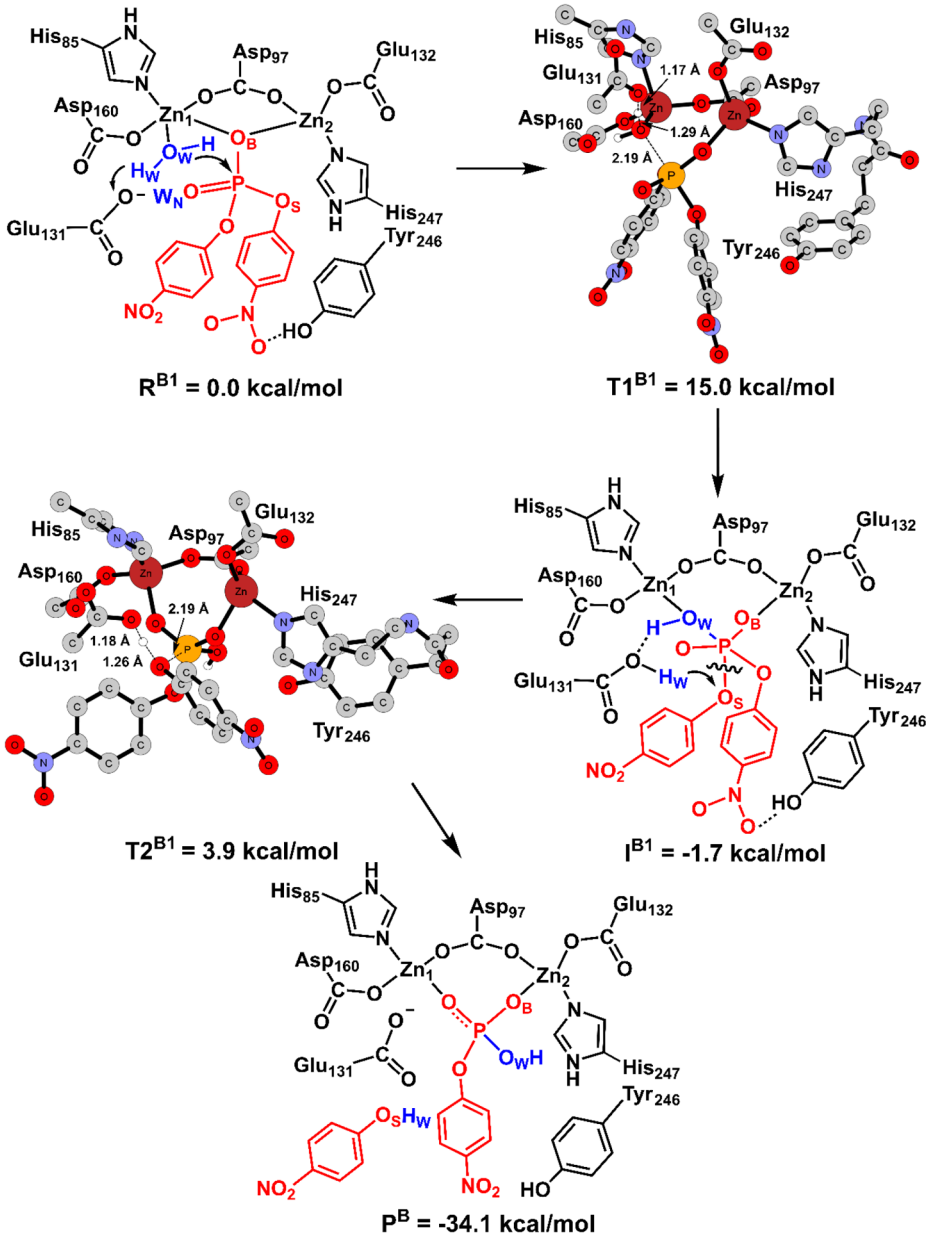

Figure 4. Mechanism of the BNPP hydrolysis in the M1^B pathway.

M1^B Pathway. In this associative pathway, the nucleophile from the W_N water is created at the Zn_1 site (Figure 4). In the reactant ($\mathbf{R}^{B1}$), BNPP binds to the binuclear core in an asymmetric bridging mode to both Zn ions. Its interaction with the Zn_1 site is stronger than the association with the Zn_2 site (Zn_1-O_B = 2.08 Å and Zn_2-O_B = 2.21 Å, Table 2). In contrast to the strengthening of the peptide bond of Leu-*p*NA upon metal binding, the scissile O_S-P bond of BNPP in $\mathbf{R}^{B1}$ gets significantly elongated by 0.08 Å than the corresponding bond in its free form due to double Lewis acid activation (O_S-P = 1.79 Å). Here, the scissile bond gets activated, and the central P atom of BNPP becomes more electrophilic due to the binding to the binuclear metal core of the enzyme. The Zn_1-Zn_2 distance of 3.67 Å in $\mathbf{R}^{B1}$ is slightly shorter than the corresponding distance (3.69 Å) in $\mathbf{R}^{L3}$ (Tables 1 and 2). Additionally, W_N is more tightly attached to the Zn_1 ion in $\mathbf{R}^{B1}$ than in $\mathbf{R}^{L3}$, but it is less activated (Zn_1-O_W = 2.01 Å and O_W-H_W = 1.02 Å in Table 2). It is also polarized by a strong hydrogen bond by Glu_{131} ($Glu_{131}-H_W$ = 1.49 Å). Similar to Leu-*p*NA, BNPP is also stabilized by Tyr_{246} through a hydrogen bond with its *p*-nitrophenol group.

In the first step, from $\mathbf{R}^{B1}$, Glu_{131} functions as a base and abstracts the H_W proton from the Zn_1 bound W_N. This proton transfer process takes place with the simultaneous attack of the $-O_WH$ nucleophile to the electrophilic phosphorus atom. This concerted process occurs with a barrier of 15.0 kcal/mol. Thus, the first step of BNPP hydrolysis is dominated by its double Lewis acid activation, while Leu-*p*NA hydrolysis is dominated by stronger nucleophilicity of the metal bound $-O_WH$ group. In general, they are competing effects, and these two reactions catalyzed by *Sg*AP provide an ideal system to study their influences. Furthermore, in contrast to the second step in the Leu-*p*NA hydrolysis, this step is clearly the rate-limiting step of the mechanism. This suggests that the chemical nature of the

https://doi.org/10.1021/acs.jcim.2c00214
J. Chem. Inf. Model. 2022, 62, 2466−2480

Table 2. Key Bond Distances (in Å) in Reactants, Transition States, Intermediates, and Products of BNPP Hydrolysis

$M1^B$	$\mathbf{R}^{B1}$	$\mathbf{T1}^{B1}$	$\mathbf{I}^{B1}$	$\mathbf{T2}^{B1}$	$\mathbf{P}^{B}$
Zn_1-Zn_2	3.67	3.86	3.96	4.30	4.34
Zn_1-O_W	2.01	2.10	2.09	3.73	3.68
Zn_2-O_W	3.78	3.80	4.04	4.06	4.44
O_W-H_W	1.02	1.29	1.54	3.11	7.85
$Glu_{131}-H_W$	1.49	1.17	1.02	1.18	1.25
Zn_1-O_B	2.08	3.49	3.25	4.02	3.80
Zn_2-O_B	2.21	1.93	1.95	2.00	2.05
O_W-P	2.77	2.19	1.84	1.74	1.72
O_S-P	1.79	1.85	2.00	2.38	6.01
$M2^B$	$\mathbf{R}^{B2}$	$\mathbf{T1}^{B2}$	$\mathbf{I}^{B2}$	$\mathbf{T2}^{B2}$	$\mathbf{P}^{B}$
Zn_1-Zn_2	3.58	3.67	3.58	3.91	4.34
Zn_1-O_W	4.70	4.35	4.24	3.61	4.44
Zn_2-O_W	2.08	2.10	2.30	2.12	3.68
O_W-H_W	1.03	1.20	1.57	0.98	7.85
$Glu_{131}-H_W$	1.49	1.22	1.03	1.25	1.25
Zn_1-O_B	2.08	2.02	2.04	3.49	3.80
Zn_2-O_B	2.23	2.33	2.10	1.98	2.05
O_W-P	3.28	2.40	1.90	1.76	1.72
O_S-P	1.78	1.75	1.82	2.36	6.01
$M12^{BOH}$	$\mathbf{R}^{BOH}$	$\mathbf{T1}^{BOH}$	$\mathbf{I}^{BOH}$	–	–
Zn_1-Zn_2	3.43	3.65	4.24	–	–
Zn_1-O_W	1.96	2.09	2.02	–	–
Zn_2-O_W	2.00	2.36	3.89	–	–
Zn_1-O_B	5.05	4.12	3.77	–	–
Zn_2-O_B	2.09	2.05	1.96	–	–
O_W-P	4.75	1.90	1.65	–	–
O_S-P	1.72	1.97	5.05	–	–

substrate determines energetics of the nucleophile generation and its attack on the electrophile. The trigonal bipyramidal phosphorane intermediate ($\mathbf{I}^{B1}$) formed in this step is slightly exergonic by 1.7 kcal/mol. In comparison to $\mathbf{R}^{B1}$, the Zn_1-Zn_2 distance (3.96 Å) in $\mathbf{I}^{B1}$ is significantly elongated by 0.29 Å. Quite interestingly, this bond follows the opposite pattern in the first step for both substrates; i.e., it elongates for BNPP and shrinks for Leu-*p*NA after the $\mathbf{R}^{L3} \rightarrow \mathbf{R}^{L1}$ transformation (Table 1). The Zn_1-O_W distance in $\mathbf{R}^{B1}$ becomes much shorter by 0.18 Å than the corresponding distance in $\mathbf{R}^{L3}$ (Tables 1 and 2) and increases the barrier for the nucleophilic attack. In $\mathbf{I}^{B1}$, the O_S-P bond is significantly activated by 0.21 Å due to the formation of the O_W-P bond (O_S-P = 2.0 Å and O_W-P = 1.84 Å in Table 2). It is also stabilized through hydrogen bonding by Tyr_{246} and Asp_{160}. In the next step, donation of the H_w proton by neutral Glu_{131} to the O_S atom of BNPP cleaves its O_S-P bond. It takes places through transition state ($\mathbf{T2}^{B1}$) with a small barrier of 5.6 kcal/mol from $\mathbf{I}^{B1}$, i.e., 3.9 kcal/mol from $\mathbf{R}^{B1}$. In comparison, cleavage of the peptide bond of Leu-*p*NA occurs with a significantly higher barrier of 15.1 kcal/mol. In comparison to $\mathbf{I}^{B1}$, the O_S-P bond in $\mathbf{T2}^{B1}$ is even more elongated (O_S-P = 2.38 Å). In the final product ($\mathbf{P}^{B}$), free *p*-nitrophenol and *p*-nitrophenyl phosphate fragments are formed. They are bound in the same fashion as the phosphate ion in the crystal structure,[74] and $\mathbf{P}^{B}$ is exergonic by 34.1 kcal/mol from $\mathbf{R}^{B1}$.

It is noteworthy that both steps of the mechanism can also occur in a single step in a concerted form of the dissociative–associative mechanism (Figure S6). In a S_N2-like reaction, the inline nucleophilic attack occurs concomitantly with the cleavage of the O_S-P bond. All key coordinates in the transition state ($\mathbf{TC}^{B1}$ in Figure S6) confirm the concerted nature of this process. The nucleophile–electrophile distance (O_W-P_S) is 1.99 Å, while the O_S-P distance is 1.94 Å, 0.1 Å longer than the same distance in $\mathbf{T1}^{B1}$. The sum of O_W-P and O_S-P bonds of 3.93 Å suggests that $\mathbf{TC}^{B1}$ is slightly tighter than $\mathbf{T1}^{B1}$. However, this pathway occurs with a barrier of 16.7 kcal/mol, which is 1.7 kcal/mol higher than the rate-limiting barrier (15.0 kcal/mol) computed for the associative pathway.

The computed energetics suggest that, unlike Leu-*p*NA, BNPP utilizes double Lewis activation for its hydrolysis. The associative pathway is energetically more favorable than the synchronous mechanism. In the former, the first step involving nucleophilic activation and its attack on the electrophilic phosphate is the rate-determining step of the mechanism.

$M2^B$ Pathway. The BNPP hydrolysis can also take place through another associative $M2^B$ pathway in which the nucleophile is created at the Zn_2 site (Figure 5). The reactant ($\mathbf{R}^{B2}$) in this pathway is slightly exergonic by 1.8 kcal/mol in comparison to $\mathbf{R}^{B1}$. In $\mathbf{R}^{B2}$, like in $\mathbf{R}^{B1}$, BNPP asymmetrically interacts with both metal ions, but its interaction with Zn_1 is much stronger than the one with Zn_2 (Zn_1-O_B = 2.08 Å and Zn_2-O_B = 2.23 Å, Table 2). However, the Zn_1-Zn_2 distance of 3.58 Å in $\mathbf{R}^{B2}$ is also substantially (0.09 Å) shorter than the corresponding distance in $\mathbf{R}^{B1}$. The Zn_2-W_N association in $\mathbf{R}^{B2}$ is weaker than the Zn_1-W_N interaction in $\mathbf{R}^{B1}$ (Zn_1-O_W = 2.01 Å and Zn_2-O_W = 2.08 Å, Table 2). The W_N is slightly (0.01 Å) more activated in $\mathbf{R}^{B2}$ than in $\mathbf{R}^{B1}$ (O_W-H_W = 1.03 Å, Table 2). However, the lengths of the scissile O_S-P bonds of BNPP in $\mathbf{R}^{B1}$ and $\mathbf{R}^{B2}$ are exactly the same (O_S-P = 1.78 Å) due to the double Lewis acid activation in both cases. Similar to $\mathbf{R}^{B1}$, the BNPP binding is also facilitated through a hydrogen bond by Tyr_{246}.

In the first step, abstraction of the H_w proton from the Zn_2 bound W_N by Glu_{131} occurs synchronously with the nucleophilic attack by the $-O_WH$ group to BNPP. The barrier for this concerted process is 16.8 kcal/mol from $\mathbf{R}^{B2}$. Since $\mathbf{R}^{B2}$ is 1.8 kcal/mol more exergonic than $\mathbf{R}^{B1}$, a pathway starting from the former and continuing through the $M1^B$ pathway will also occur through exactly the same barrier (Figure 6). The computed barriers of 16.8 kcal/mol for both these pathways are in excellent agreement with the measured value of 18.3 kcal/mol.[66] The formation of the $\mathbf{I}^{B2}$ intermediate is more endergonic by 3.6 kcal/mol. In comparison, the creation of the corresponding intermediate in the $M1^B$ pathway is slightly exergonic by 1.7 kcal/mol. From $\mathbf{I}^{B2}$, the donation of the previously acquired H_w proton by Glu_{131} to the O_S atom of the substrate cleaves the O_S-P bond and releases the nitrophenolate group in the final product ($\mathbf{P}^{B}$). This process takes place with a small barrier of 2.5 kcal/mol from $\mathbf{I}^{B2}$, i.e., 6.1 kcal/mol from $\mathbf{R}^{B2}$. Similar to the $M1^B$ pathway, this pathway can also take place in an S_N2 reaction-like dissociative manner (Figure S7). However, the barrier of 27.1 kcal/mol for this process is prohibitively high.

These results suggest that the first step is the rate-limiting step of the mechanism. The pathways starting from $\mathbf{R}^{B2}$ ($M2^B$ pathway) and $\mathbf{R}^{B2} \rightarrow \mathbf{R}^{B1}$ ($M1^B$ pathway) are equally plausible with the barriers of 16.8 kcal/mol.

$M12^{BOH}$ pathway. In the reactant ($\mathbf{R}^{BOH}$) of this dissociative pathway (Figure S8), the hydroxyl nucleophile (μ-O_WH_W) is bridging both metal centers in an asymmetric fashion. In $\mathbf{R}^{BOH}$, the Zn_1-O_W bond is stronger than the Zn_2-O_W bond (Zn_1-O_W = 1.96 Å and Zn_2-O_W = 2.00 Å, Table 2). The Zn_1-Zn_2 distance of 3.43 Å in $\mathbf{R}^{BOH}$ is the shortest among

https://doi.org/10.1021/acs.jcim.2c00214
J. Chem. Inf. Model. 2022, 62, 2466–2480

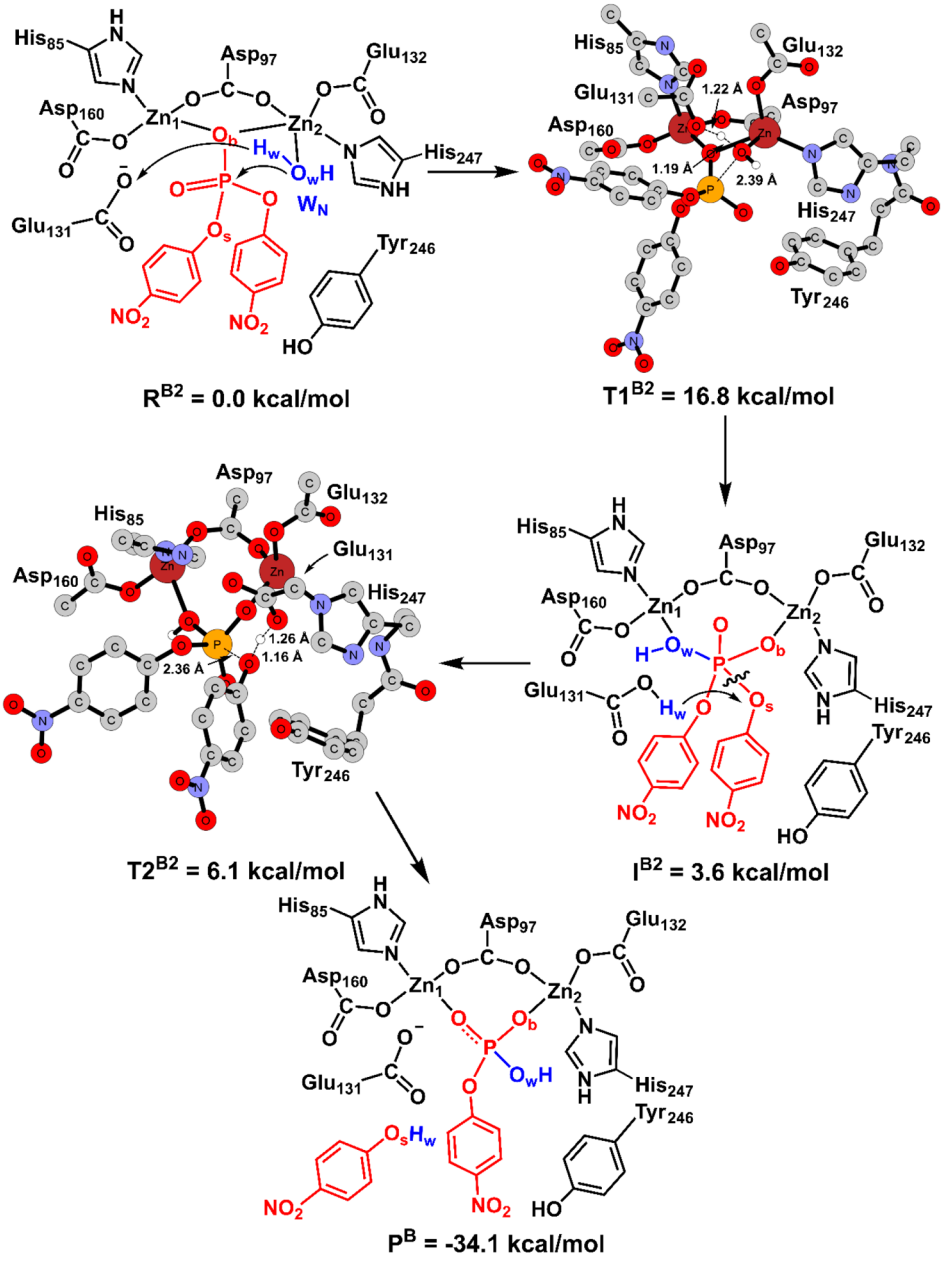

Figure 5. Mechanism of the BNPP hydrolysis in the $M2^B$ pathway.

all the reactants for this substrate (Table 2). Here, in a concerted manner, the μ-O_WH_W group attacks the P atom of BNPP and cleaves the O_S−P bond of the *p*-nitrophenol group stabilized by Tyr_{246}. In the transition state ($\mathbf{TC}^{\mathbf{BOH}}$), a shorter Zn_1−O_W distance suggests that the nucleophile is delivered primarily by the Zn_1 site (Zn_1−O_W = 2.09 Å and Zn_2−O_W = 2.36 Å, Table 2). This pathway occurs with a barrier of 30.5 kcal/mol that is the highest among all mechanisms investigated in this study. Therefore, it is ruled out.

SUMMARY AND CONCLUSIONS

In this DFT study, the chemical promiscuity of *Sg*AP in catalyzing peptide and phosphoester hydrolyses is investigated using Leu-*p*NA and BNPP as substrates, respectively. In particular, four ($M1^L$, $M2^L$, $M12^L$, and $M12^{LOH}$) distinct pathways for LeuAP and three ($M1^B$, $M2^B$, and $M12^{BOH}$) pathways for BNPP are explored. The potential energy diagrams of the most plausible mechanisms are shown in Figures 3, 5, and 6.

The computed energetics of all four pathways suggest a hybrid mechanism for the Leu-*p*NA hydrolysis (Figure 3). In the reactant ($\mathbf{R}^{\mathbf{L3}}$) for this mechanism, the nucleophile-generating water (W_N) is bound in a bridging manner to both metals. This binding mode is supported by the fluoride inhibition experiments.[83] This reactant can subsequently transform into $\mathbf{R}^{\mathbf{L1}}$ in which W_N water is coordinated only to the Zn_1 ion. This structure is 5.1 kcal/mol more endergonic than $\mathbf{R}^{\mathbf{L3}}$. The overall barrier of 16.5 kcal/mol for this mechanism from $\mathbf{R}^{\mathbf{L3}}$ is in the good agreement with the measured value of 13.9 kcal/mol.[66] The second step associated with the cleavage of the peptide bond is likely to be the rate-limiting step of the mechanism. As suggested by the measured

https://doi.org/10.1021/acs.jcim.2c00214
J. Chem. Inf. Model. 2022, 62, 2466−2480

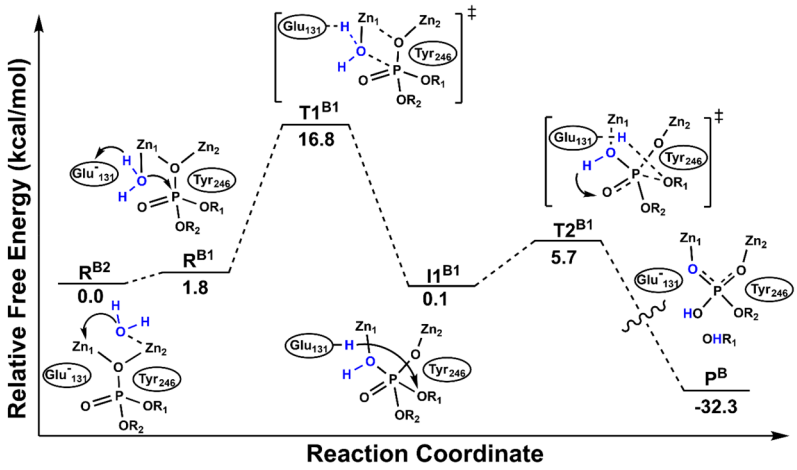

Figure 6. Plausible mechanism for the BNPP hydrolysis by *Sg*AP. The arrows describe the transfer of atoms.

solvent isotope effects,[83] this reaction involves transfer of two protons. There is no double Lewis acid activation of the substrate, and the nucleophilicity of the hydroxyl ion plays a critical role in the reaction. This could be one of the factors why peptide hydrolysis can be catalyzed by both mononuclear and binuclear metal cofactors containing hydrolases.

On the other hand, the computed energetics suggest that BNPP hydrolysis is likely to be initiated from $\mathbf{R^{B2}}$, and both $M2^{B}$ and $\mathbf{R^{B2}} \rightarrow \mathbf{R^{B1}}$ ($M1^{B}$ pathway) pathways are equally favored (Figures 5 and 6). The barriers of 16.8 kcal/mol for both these pathways are in excellent agreement with the measured value of 18.3 kcal/mol.[66] The first step involving nucleophilic activation and its attack on the electrophilic phosphorus atom is the rate-determining step of the mechanism. The associative pathway is found to be energetically more favorable than its synchronous counterpart. As observed experimentally,[83] BNPP hydrolysis involves a single-proton transfer step. In contrast to Leu-*p*NA, BNPP hydrolysis utilized double Lewis acid activation. This could be the major reason for the necessity of a binuclear metal core for phosphoester hydrolysis. These results have provided intricate details of the chemical promiscuity of this interesting enzyme.

DATA AND SOFTWARE AVAILABILITY

The enzyme−substrate models were built through molecular docking using the open source AutoDock Vina 1.5.6 software. All DFT calculations using these models were performed using the Gaussian 16 software. The details of these methods and software including relevant citations are provided in the Computational Details section. The Cartesian coordinates of all optimized structures are provided as Supporting Information.

ASSOCIATED CONTENT

Supporting Information

The Supporting Information is available free of charge at https://pubs.acs.org/doi/10.1021/acs.jcim.2c00214.

Figures S1−S8 and Cartesian coordinates of all optimized structures(PDF)

AUTHOR INFORMATION

Corresponding Author

Rajeev Prabhakar − *Department of Chemistry, University of Miami, Coral Gables, Florida 33146, United States;* orcid.org/0000-0003-1137-1272; Phone: 305-284-9372; Email: rpr@miami.edu; Fax: 305-284-4571

Authors

Leonardo F. Serafim − *Department of Chemistry, University of Miami, Coral Gables, Florida 33146, United States*

Vindi M. Jayasinghe-Arachchige − *Department of Chemistry, University of Miami, Coral Gables, Florida 33146, United States*

Lukun Wang − *Department of Chemistry, University of Miami, Coral Gables, Florida 33146, United States*

Complete contact information is available at: https://pubs.acs.org/10.1021/acs.jcim.2c00214

Notes

The authors declare no competing financial interest.

ACKNOWLEDGMENTS

This material is based upon work supported by a grant from the National Science Foundation (Grant No. CHE- 2102563) to R.P. Computational resources from the University of Miami Institute for Data Science & Computing (IDSC) are greatly acknowledged.

REFERENCES

(1) Serafim, L. F.; Wang, L.; Rathee, P.; Yang, J.; Frenk Knaul, H. S.; Prabhakar, R. Remediation of Environmentally Hazardous Organophosphates by Artificial Metalloenzymes. *Curr. Opin. Green Sustain. Chem.* **2021**, *32*, 100529.

(2) Hu, Q.; Jayasinghe-Arachchige, V. M.; Sharma, G.; Serafim, L. F.; Paul, T. J.; Prabhakar, R. Mechanisms of Peptide and Phosphoester Hydrolysis Catalyzed by Two Promiscuous Metalloenzymes (Insulin Degrading Enzyme and Glycerophosphodiesterase) and Their Synthetic Analogues. *Wiley Interdiscip. Rev. Comput. Mol. Sci.* **2020**, *10*, e1466.

(3) Bakhtiar, R.; Thomas, J. J.; Siuzdak, G. Mass Spectrometry in Viral Proteomics. *Acc. Chem. Res.* **2000**, *33*, 179−187.

(4) Beynon, R.; Bond, J. S. *Proteolytic Enzymes: a Practical Approach*; OUP: Oxford, 2001; Vol. *247*.

(5) Lassila, J. K.; Zalatan, J. G.; Herschlag, D. Biological Phosphoryl-Transfer Reactions: Understanding Mechanism and Catalysis. *Annu. Rev. Biochem.* **2011**, *80*, 669−702.
(6) Weston, J. Mode of Action of Bi-and Trinuclear Zinc Hydrolases and Their Synthetic Analogues. *Chem. Rev.* **2005**, *105*, 2151−2174.
(7) Mitic, N.; Smith, S. J.; Neves, A.; Guddat, L. W.; Gahan, L. R.; Schenk, G. The Catalytic Mechanisms of Binuclear Metallohydrolases. *Chem. Rev.* **2006**, *106*, 3338−63.
(8) Simon, M. I.; Thorner, J.; Emr, S. D.; Abelson, J. N. *Applications of Chimeric Genes and Hybrid Proteins, Part A: Gene Expression and Protein Purification*; Elsevier, 2000.
(9) Heyduk, T.; Baichoo, N.; Heyduk, E. Hydroxyl Radical Footprinting of Proteins Using Metal Ion Complexes. *Met. Ions Biol. Syst.* **2001**, *38*, 255−288.
(10) Suh, J. Model Studies of Metalloenzymes Involving Metal Ions as Lewis Acid Catalysts. *Acc. Chem. Res.* **1992**, *25*, 273−279.
(11) Lee, T. Y.; Suh, J. Target-Selective Peptide-Cleaving Catalysts as a New Paradigm in Drug Design. *Chem. Soc. Rev.* **2009**, *38*, 1949−1957.
(12) Suh, J.; Yoo, S. H.; Kim, M. G.; Jeong, K.; Ahn, J. Y.; Kim, M. S.; Chae, P. S.; Lee, T. Y.; Lee, J.; Lee, J.; Jang, Y. A.; Ko, E. H. Cleavage Agents for Soluble Oligomers of Amyloid Beta Peptides. *Angew. Chem., Int. Ed.* **2007**, *46*, 7064−7.
(13) Meggers, E. Targeting Proteins with Metal Complexes. *Chem. Commun. (Cambridge, U. K.)* **2009**, 1001−10.
(14) Daumann, L. J.; Larrabee, J. A.; Ollis, D.; Schenk, G.; Gahan, L. R. Immobilization of the Enzyme GpdQ on Magnetite Nanoparticles for Organophosphate Pesticide Bioremediation. *J. Inorg. Biochem.* **2014**, *131*, 1−7.
(15) Schenk, G.; Mitic, N.; Gahan, L. R.; Ollis, D. L.; McGeary, R. P.; Guddat, L. W. Binuclear Metallohydrolases: Complex Mechanistic Strategies for a Simple Chemical Reaction. *Acc. Chem. Res.* **2012**, *45*, 1593−603.
(16) Ghanem, E.; Li, Y.; Xu, C.; Raushel, F. M. Characterization of a Phosphodiesterase Capable of Hydrolyzing EA 2192, the Most Toxic Degradation Product of the Nerve Agent VX. *Biochemistry* **2007**, *46*, 9032−9040.
(17) Katz, M. J.; Moon, S.-Y.; Mondloch, J. E.; Beyzavi, M. H.; Stephenson, C. J.; Hupp, J. T.; Farha, O. K. Exploiting Parameter Space in MOFs: a 20-fold Enhancement of Phosphate-ester Hydrolysis with UiO-66-NH 2. *Chem. Sci.* **2015**, *6*, 2286−2291.
(18) Galante, Y. M.; Formantici, C. Enzyme Applications in Detergency and in Manufacturing Industries. *Curr. Org. Chem.* **2003**, *7*, 1399−1422.
(19) Rao, M. B.; Tanksale, A. M.; Ghatge, M. S.; Deshpande, V. V. Molecular and Biotechnological Aspects of Microbial Proteases. *Microbiol. Mol. Biol. Rev.* **1998**, *62*, 597−635.
(20) Gewert, B.; Plassmann, M. M.; MacLeod, M. Pathways for Degradation of Plastic Polymers Floating in the Marine Environment. *Environ. Sci. Process. Impacts* **2015**, *17*, 1513−21.
(21) Schenk, G.; Mateen, I.; Ng, T.-K.; Pedroso, M. M.; Mitić, N.; Jafelicci, M., Jr; Marques, R. F.; Gahan, L. R.; Ollis, D. L. Organophosphate-Degrading Metallohydrolases: Structure and Function of Potent Catalysts for Applications in Bioremediation. *Coord. Chem. Rev.* **2016**, *317*, 122−131.
(22) Bezborodov, A. M.; Zagustina, N. A. Enzymatic Biocatalysis in Chemical Synthesis of Pharmaceuticals. *Prikl. Biokhim. Mikrobiol.* **2016**, *52*, 257−271.
(23) Sang, Q. X. Complex Role of Matrix Metalloproteinases in Angiogenesis. *Cell Res.* **1998**, *8*, 171−7.
(24) Juliano, S. A.; Serafim, L. F.; Duay, S. S.; Heredia Chavez, M.; Sharma, G.; Rooney, M.; Comert, F.; Pierce, S.; Radulescu, A.; Cotten, M. L.; Mihailescu, M.; May, E. R.; Greenwood, A. I.; Prabhakar, R.; Angeles-Boza, A. M. A Potent Host Defense Peptide Triggers DNA Damage and is Active Against Multidrug-Resistant Gram-Negative Pathogens. *ACS Infect. Dis.* **2020**, *6*, 1250−1263.
(25) Frenkel-Pinter, M.; Samanta, M.; Ashkenasy, G.; Leman, L. J. Prebiotic Peptides: Molecular Hubs in the Origin of Life. *Chem. Rev.* **2020**, *120*, 4707−4765.
(26) Aboelnga, M. M.; Wetmore, S. D. Unveiling a Single-Metal-Mediated Phosphodiester Bond Cleavage Mechanism for Nucleic Acids: A Multiscale Computational Investigation of a Human DNA Repair Enzyme. *J. Am. Chem. Soc.* **2019**, *141*, 8646−8656.
(27) Boneta, S.; Arafet, K.; Moliner, V. QM/MM Study of the Enzymatic Biodegradation Mechanism of Polyethylene Terephthalate. *J. Chem. Inf. Model* **2021**, *61*, 3041−3051.
(28) Kamerlin, S. C.; Sharma, P. K.; Prasad, R. B.; Warshel, A. Why Nature Really Chose Phosphate. *Q. Rev. Biophys.* **2013**, *46*, 1−132.
(29) Saha, K.; R, U. M.; Sikder, J.; Chakraborty, S.; da Silva, S. S.; dos Santos, J. C. Membranes as a Tool to Support Biorefineries: Applications in Enzymatic Hydrolysis, Fermentation and Dehydration for Bioethanol Production. *Renew. Sust. Energy Rev.* **2017**, *74*, 873−890.
(30) Gänzle, M. G.; Haase, G.; Jelen, P. Lactose: Crystallization, Hydrolysis and Value-Added Derivatives. *Int. Dairy J.* **2008**, *18*, 685−694.
(31) Yu, Y.; Lou, X.; Wu, H. Some Recent Advances in Hydrolysis of Biomass in Hot-Compressed Water and Its Comparisons with Other Hydrolysis Methods. *Energy Fuels* **2008**, *22*, 46−60.
(32) Pierre, T. S.; Chiellini, E. Biodegradability of Synthetic Polymers for Medical and Pharmaceutical Applications: Part 2—Backbone Hydrolysis. *J. Bioact. Compat. Polym.* **1987**, *2*, 4−30.
(33) Ügdüler, S.; Van Geem, K. M.; Denolf, R.; Roosen, M.; Mys, N.; Ragaert, K.; De Meester, S. Towards Closed-loop Recycling of Multilayer and Coloured PET Plastic Waste by Alkaline Hydrolysis. *Green Chem.* **2020**, *22*, 5376−5394.
(34) Masbou, J.; Drouin, G.; Payraudeau, S.; Imfeld, G. Carbon and Nitrogen Stable Isotope Fractionation during Abiotic Hydrolysis of Pesticides. *Chemosphere* **2018**, *213*, 368−376.
(35) Lv, H.; Geletii, Y. V.; Zhao, C.; Vickers, J. W.; Zhu, G.; Luo, Z.; Song, J.; Lian, T.; Musaev, D. G.; Hill, C. L. Polyoxometalate Water Oxidation Catalysts and the Production of Green Fuel. *Chem. Soc. Rev.* **2012**, *41*, 7572−89.
(36) Bachman, A. B.; Keramisanou, D.; Xu, W.; Beebe, K.; Moses, M. A.; Vasantha Kumar, M. V.; Gray, G.; Noor, R. E.; van der Vaart, A.; Neckers, L.; Gelis, I. Phosphorylation Induced Cochaperone Unfolding Promotes Kinase Recruitment and Client Class-Specific Hsp90 Phosphorylation. *Nat. Commun.* **2018**, *9*, 265.
(37) Lengyel, Z.; Rufo, C. M.; Moroz, Y. S.; Makhlynets, O. V.; Korendovych, I. V. Copper-Containing Catalytic Amyloids Promote Phosphoester Hydrolysis and Tandem Reactions. *ACS Catal.* **2018**, *8*, 59−62.
(38) Pecina, A.; Rosa-Gastaldo, D.; Riccardi, L.; Franco-Ulloa, S.; Milan, E.; Scrimin, P.; Mancin, F.; De Vivo, M. On the Metal-Aided Catalytic Mechanism for Phosphodiester Bond Cleavage Performed by Nanozymes. *ACS Catal.* **2021**, *11*, 8736−8748.
(39) Afrose, S. P.; Ghosh, C.; Das, D. Substrate Induced Generation of Transient Self-Assembled Catalytic Systems. *Chem. Sci.* **2021**, *12*, 14674−14685.
(40) Groß, C.; Hamacher, K.; Schmitz, K.; Jager, S. Cleavage Product Accumulation Decreases the Activity of Cutinase during PET Hydrolysis. *J. Chem. Inf. Model* **2017**, *57*, 243−255.
(41) Radzicka, A.; Wolfenden, R. Rates of Uncatalyzed Peptide Bond Hydrolysis in Neutral Solution and the Transition State Affinities of Proteases. *J. Am. Chem. Soc.* **1996**, *118*, 6105−6109.
(42) Wolfenden, R. Benchmark Reaction Rates, the Stability of Biological Molecules in Water, and the Evolution of Catalytic Power in Enzymes. *Annu. Rev. Biochem.* **2011**, *80*, 645−67.
(43) Lipscomb, W. N.; Strater, N. Recent Advances in Zinc Enzymology. *Chem. Rev.* **1996**, *96*, 2375−2434.
(44) Paetzel, M.; Karla, A.; Strynadka, N. C.; Dalbey, R. E. Signal Peptidases. *Chem. Rev.* **2002**, *102*, 4549−80.
(45) Powers, J. C.; Asgian, J. L.; Ekici, O. D.; James, K. E. Irreversible Inhibitors of Serine, Cysteine, and Threonine Proteases. *Chem. Rev.* **2002**, *102*, 4639−750.
(46) Shen, Y.; Joachimiak, A.; Rosner, M. R.; Tang, W. J. Structures of Human Insulin-Degrading Enzyme Reveal a New Substrate Recognition Mechanism. *Nature* **2006**, *443*, 870−874.

https://doi.org/10.1021/acs.jcim.2c00214
J. Chem. Inf. Model. 2022, 62, 2466−2480

(47) Sträter, N.; Lipscomb, W. N. Transition State Analogue L-Leucinephosphonic Acid Bound to Bovine Lens Leucine Aminopeptidase: X-Ray Structure at 1.65 Å Resolution in a New Crystal Form. *Biochemistry* **1995**, *34*, 9200−9210.
(48) Tong, L. Viral Proteases. *Chem. Rev.* **2002**, *102*, 4609−26.
(49) Tanaka, F. Catalytic Antibodies as Designer Proteases and Esterases. *Chem. Rev.* **2002**, *102*, 4885−4906.
(50) Devamani, T.; Rauwerdink, A. M.; Lunzer, M.; Jones, B. J.; Mooney, J. L.; Tan, M. A.; Zhang, Z. J.; Xu, J. H.; Dean, A. M.; Kazlauskas, R. J. Catalytic Promiscuity of Ancestral Esterases and Hydroxynitrile Lyases. *J. Am. Chem. Soc.* **2016**, *138*, 1046−56.
(51) Sacher, O.; Reitz, M.; Gasteiger, J. Investigations of Enzyme-Catalyzed Reactions Based on Physicochemical Descriptors Applied to Hydrolases. *J. Chem. Inf. Model* **2009**, *49*, 1525−1534.
(52) Chen, B.; Kang, Z.; Zheng, E.; Liu, Y.; Gauld, J. W.; Wang, Q. Hydrolysis Mechanism of the Linkers by Matrix Metalloproteinase-9 Using QM/MM Calculations. *J. Chem. Inf. Model* **2021**, *61*, 5203−5211.
(53) Borosky, G. L.; Lin, S. Computational Modeling of the Catalytic Mechanism of Human Placental Alkaline Phosphatase (PLAP). *J. Chem. Inf. Model* **2011**, *51*, 2538−2548.
(54) Borosky, G. L. Quantum-Mechanical Study on the Catalytic Mechanism of Alkaline Phosphatases. *J. Chem. Inf. Model* **2017**, *57*, 540−549.
(55) Lai, R.; Tang, W.-J.; Li, H. Catalytic Mechanism of Amyloid-β Peptide Degradation by Insulin Degrading Enzyme: Insights from Quantum Mechanics and Molecular Mechanics Style Møller−Plesset Second Order Perturbation Theory Calculation. *J. Chem. Inf. Model.* **2018**, *58*, 1926−1934.
(56) Feinberg, H.; Greenblatt, H. M.; Shoham, G. Structural Studies of the Role of the Active Site Metal in Metalloenzymes. *J. Chem. Inf. Comput. Sci.* **1993**, *33*, 501−516.
(57) Pope, D.; Madura, J. D.; Cascio, M. β-Amyloid and Neprilysin Computational Studies Identify Critical Residues Implicated in Binding Specificity. *J. Chem. Inf. Model* **2014**, *54*, 1157−1165.
(58) Dunn, B. M. Structure and Mechanism of the Pepsin-Like Family of Aspartic Peptidases. *Chem. Rev.* **2002**, *102*, 4431−58.
(59) Hu, Q.; Jayasinghe-Arachchige, V. M.; Prabhakar, R. Degradation of a Main Plastic Pollutant Polyethylene Terephthalate by Two Distinct Proteases (Neprilysin and Cutinase-Like Enzyme). *J. Chem. Inf. Model* **2021**, *61*, 764−776.
(60) Matthews, B. W. Structural Basis of the Action of Thermolysin and Related Zinc Peptidases. *Acc. Chem. Res.* **1988**, *21*, 333−340.
(61) Polgár, L. The Catalytic Triad of Serine Peptidases. *Cell. Mol. Life Sci.* **2005**, *62*, 2161−2172.
(62) Fahs, S.; Lujan, P.; Köhn, M. Approaches to Study Phosphatases. *ACS Chem. Biol.* **2016**, *11*, 2944−2961.
(63) Köhn, M. Turn and Face the Strange: A New View on Phosphatases. *ACS Cent. Sci.* **2020**, *6*, 467−477.
(64) Turk, B. Targeting Proteases: Successes, Failures and Future Prospects. *Nat. Rev. Drug Discovery* **2006**, *5*, 785−799.
(65) Park, H. I.; Ming, L. J. A 10^{10} Rate Enhancement of Phosphodiester Hydrolysis by a Dinuclear Aminopeptidase—Transition-State Analogues as Substrates? *Angew. Chem., Int. Ed.* **1999**, *38*, 2914−2916.
(66) Ercan, A.; Park, H. I.; Ming, L. J. A "Moonlighting" Dizinc Aminopeptidase from *Streptomyces griseus*: Mechanisms for Peptide Hydrolysis and the 4 × 10(10)-fold Acceleration of the Alternative Phosphodiester Hydrolysis. *Biochemistry* **2006**, *45*, 13779−93.
(67) Ercan, A.; Tay, W. M.; Grossman, S. H.; Ming, L.-J. Mechanistic Role of Each Metal Ion in Streptomyces Dinuclear Aminopeptidase: Peptide Hydrolysis and 7× 10^{10}-fold Rate Enhancement of Phosphodiester Hydrolysis. *J. Inorg. Biochem.* **2010**, *104*, 19−29.
(68) Taylor, A. Aminopeptidases: Structure and Function. *FASEB J.* **1993**, *7*, 290−298.
(69) Gonzales, T.; Robert-Baudouy, J. Bacterial Aminopeptidases: Properties and Functions. *FEMS Microbiol. Rev.* **1996**, *18*, 319−344.
(70) Rawlings, N. D.; Salvesen, G. *Handbook of Proteolytic Enzymes*; Academic Press, 2013; Vol. *3*.
(71) Mitic, N.; Miraula, M.; Selleck, C.; Hadler, K. S.; Uribe, E.; Pedroso, M. M.; Schenk, G. Catalytic Mechanisms of Metallohydrolases Containing Two Metal Ions. *Adv. Protein Chem. Struct. Biol.* **2014**, *97*, 49−81.
(72) Melbye, S. W.; Carpenter, F. H. Leucine Aminopeptidase (Bovine lens). Stability and Size of Subunits. *J. Biol. Chem.* **1971**, *246*, 2459−63.
(73) Holz, R. C. The Aminopeptidase from Aeromonas Proteolytica: Structure and Mechanism of Co-catalytic Metal Centers Involved in Peptide Hydrolysis. *Coord. Chem. Rev.* **2002**, *232*, 5−26.
(74) Greenblatt, H. M.; Almog, O.; Maras, B.; Spungin-Bialik, A.; Barra, D.; Blumberg, S.; Shoham, G. *Streptomyces griseus* Aminopeptidase: X-Ray Crystallographic Structure at 1.75 Å Resolution. *J. Mol. Biol.* **1997**, *265*, 620−636.
(75) Cassano, A. G.; Anderson, V. E.; Harris, M. E. Understanding the Transition States of Phosphodiester Bond Cleavage: Insights from Heavy Atom Isotope Effects. *Biopolymers* **2004**, *73*, 110−29.
(76) Papir, G.; Spungin-Bialik, A.; Ben-Meir, D.; Fudim, E.; Gilboa, R.; Greenblatt, H. M.; Shoham, G.; Lessel, U.; Schomburg, D.; Ashkenazi, R.; Blumberg, S. Inhibition of *Streptomyces griseus* Aminopeptidase and Effects of Calcium Ions on Catalysis and Binding−Comparisons with the Homologous Enzyme *Aeromonas Proteolytica* Aminopeptidase. *Eur. J. Chem.* **1998**, *258*, 313−9.
(77) Almog, O.; Greenblatt, H. M.; Spungin, A.; Ben-Meir, D.; Blumberg, S.; Shoham, G. Crystallization and Preliminary Crystallographic Analysis of *Streptomyces griseus* Aminopeptidase. *J. Mol. Biol.* **1993**, *230*, 342−4.
(78) Greenblatt, H.; Almog, O.; Maras, B.; Spungin-Bialik, A.; Barra, D.; Blumberg, S.; Shoham, G. *Streptomyces griseus* Aminopeptidase: X-Ray Crystallographic Structure at 1.75 Å Resolution. *J. Mol. Biol.* **1997**, *265*, 620−636.
(79) Reiland, V.; Gilboa, R.; Spungin-Bialik, A.; Schomburg, D.; Shoham, Y.; Blumberg, S.; Shoham, G. Binding of Inhibitory Aromatic Amino Acids to *Streptomyces griseus* Aminopeptidase. *Acta Crystallogr. D* **2004**, *60*, 1738−46.
(80) Gilboa, R.; Greenblatt, H.; Perach, M.; Spungin-Bialik, A.; Lessel, U.; Wohlfahrt, G.; Schomburg, D.; Blumberg, S.; Shoham, G. Interactions of *Streptomyces griseus* Aminopeptidase with a Methionine Product Analogue: A Structural Study at 1.53 Å Resolution. *Acta Crystallogr. D* **2000**, *56*, 551−558.
(81) Fundoiano-Hershcovitz, Y.; Rabinovitch, L.; Langut, Y.; Reiland, V.; Shoham, G.; Shoham, Y. Identification of the Catalytic Residues in the Double-Zinc Aminopeptidase from *Streptomyces griseus*. *FEBS Lett.* **2004**, *571*, 192−6.
(82) Gilboa, R.; Spungin-Bialik, A.; Wohlfahrt, G.; Schomburg, D.; Blumberg, S.; Shoham, G. Interactions of *Streptomyces griseus* Aminopeptidase with Amino Acid Reaction Products and Their Implications toward a Catalytic Mechanism. *Proteins* **2001**, *44*, 490−504.
(83) Hershcovitz, Y. F.; Gilboa, R.; Reiland, V.; Shoham, G.; Shoham, Y. Catalytic Mechanism of SGAP, a Double-Zinc Aminopeptidase from *Streptomyces griseus*. *FEBS J.* **2007**, *274*, 3864−76.
(84) Harris, M. N.; Ming, L.-J. Different Phosphate Binding Modes of *Streptomyces griseus* Aminopeptidase between Crystal and Solution States and the Status of Zinc-Bound Water. *FEBS Lett.* **1999**, *455*, 321−324.
(85) O'Ferrall, R. M. Relationships between E2 and E1cB Mechanisms of β-Elimination. *J. Chem. Soc. B* **1970**, *0*, 274−277.
(86) Kirby, A. J.; Nome, F. Fundamentals of Phosphate Transfer. *Acc. Chem. Res.* **2015**, *48*, 1806−14.
(87) Duarte, F.; Åqvist, J.; Williams, N. H.; Kamerlin, S. C. Resolving Apparent Conflicts between Theoretical and Experimental Models of Phosphate Monoester Hydrolysis. *J. Am. Chem. Soc.* **2015**, *137*, 1081−1093.
(88) Alberto, M. E.; Pinto, G.; Russo, N.; Toscano, M. Triesterase and Promiscuous Diesterase Activities of a Di-CoII-Containing

https://doi.org/10.1021/acs.jcim.2c00214
J. Chem. Inf. Model. 2022, 62, 2466−2480

Organophosphate Degrading Enzyme Reaction Mechanisms. *Chem.—Eur. J.* **2015**, *21*, 3736−3745.
(89) Bigley, A. N.; Raushel, F. M. Catalytic Mechanisms for Phosphotriesterases. *Biochim. Biophys. Acta. Biomembr.* **2013**, *1834*, 443−53.
(90) Klabunde, T.; Strater, N.; Frohlich, R.; Witzel, H.; Krebs, B. Mechanism of Fe(III)-Zn(II) Purple Acid Phosphatase Based on Crystal Structures. *J. Mol. Biol.* **1996**, *259*, 737−48.
(91) Klahn, M.; Rosta, E.; Warshel, A. On the Mechanism of Hydrolysis of Phosphate Monoesters Dianions in Solutions and Proteins. *J. Am. Chem. Soc.* **2006**, *128*, 15310−23.
(92) Lopez-Canut, V.; Roca, M.; Bertran, J.; Moliner, V.; Tunon, I. Theoretical Study of Phosphodiester Hydrolysis in Nucleotide Pyrophosphatase/Phosphodiesterase. Environmental Effects on the Reaction Mechanism. *J. Am. Chem. Soc.* **2010**, *132*, 6955−63.
(93) Aubert, S. D.; Li, Y.; Raushel, F. M. Mechanism for the Hydrolysis of Organophosphates by the Bacterial Phosphotriesterase. *Biochemistry* **2004**, *43*, 5707−15.
(94) Borosky, G. L. Catalytic Activity of Human Placental Alkaline Phosphatase (PLAP): Insights from a Computational Study. *J. Phys. Chem. B* **2014**, *118*, 14302−13.
(95) Chen, S. L.; Liao, R. Z. Phosphate Monoester Hydrolysis by Trinuclear Alkaline Phosphatase; DFT Study of Transition States and Reaction Mechanism. *ChemPhysChem* **2014**, *15*, 2321−30.
(96) Kamerlin, S. C. Theoretical Comparison of P-Nitrophenyl Phosphate and Sulfate Hydrolysis in Aqueous Solution: Implications for Enzyme-Catalyzed Sulfuryl Transfer. *J. Org. Chem.* **2011**, *76*, 9228−38.
(97) Roston, D.; Cui, Q. Substrate and Transition State Binding in Alkaline Phosphatase Analyzed by Computation of Oxygen Isotope Effects. *J. Am. Chem. Soc.* **2016**, *138*, 11946−57.
(98) Zhang, H.; Yang, L.; Ding, W.; Ma, Y. The pH-Dependent Activation Mechanism of Ser102 in Escherichia Coli Alkaline Phosphatase: A Theoretical Study. *J. Biol. Inorg. Chem.* **2018**, *23*, 277−284.
(99) Zhang, H.; Yang, L.; Yan, L. F.; Liao, R. Z.; Tian, W. Q. Evolution of Phosphotriesterase Activities of the Metallo-Beta-Lactamase Family: A Theoretical Study. *J. Inorg. Biochem.* **2018**, *184*, 8−14.
(100) Sharma, G.; Jayasinghe-Arachchige, V. M.; Hu, Q.; Schenk, G.; Prabhakar, R. Effect of Chemically Distinct Substrates on the Mechanism and Reactivity of a Highly Promiscuous Metallohydrolase. *ACS Catal.* **2020**, *10*, 3684−3696.
(101) Frisch, M. J.; Trucks, G. W.; Schlegel, H. B.; Scuseria, G. E.; Robb, M. A.; Cheeseman, J. R.; Scalmani, G.; Barone, V.; Petersson, G. A.; Nakatsuji, H.; Li, X.; Caricato, M.; Marenich, A. V.; Bloino, J.; Janesko, B. G.; Gomperts, R.; Mennucci, B.; Hratchian, H. P.; Ortiz, J. V.; Izmaylov, A. F.; Sonnenber, J. L.; Williams-Young, D.; Ding, F.; Lipparini, F.; Egidi, F.; Goings, J.; Peng, B.; Petrone, A.; Henderson, T.; Ranasinghe, D.; Zakrzewsk, V. G.; Gao, J.; Rega, N.; Zheng, G.; Liang, W.; Hada, M.; Ehara, M.; Toyota, K.; Fukuda, R.; Hasegawa, J.; Ishida, M.; Nakajima, T.; Honda, Y.; Kitao, O.; Nakai, H; Vreven, T.; Throssell, K.; Montgomery, J. A., Jr.; Peralta, J. E.; Ogliaro, F.; Bearpark, M. J.; Heyd, J. J.; Brothers, E. N..; Kudin, K. N.; Staroverov, V. N.; Keith, T. A.; Kobayashi, R.; Normand, J.; Raghavachari, K.; Rendell, A. P.; Burant, J. C.; Iyengar, S. S.; Tomasi, J.; Cossi, M.; Millam, J. M.; Klene, M; Adamo, C.; Cammi, R.; Ochterski, J. W.; Martin, R. L.; Morokuma, K.; Farkas, O.; Foresman, J. B.; Fox, D. J. *Gaussian 16*, Revision B.01; Gaussian, Inc.: Wallingford, CT, 2016.
(102) Case, D. A.; Cheatham, T. E., III; Darden, T.; Gohlke, H.; Luo, R.; Merz, K. M., Jr.; Onufriev, A.; Simmerling, C.; Wang, B.; Woods, R. J. The Amber Biomolecular Simulation Programs. *J. Comput. Chem.* **2005**, *26*, 1668−1688.
(103) Trott, O.; Olson, A. J. AutoDock Vina: Improving the Speed and Accuracy of Docking with a New Scoring Function, Efficient Optimization, and Multithreading. *J. Comput. Chem.* **2010**, *31*, 455−461.
(104) MacKerell, A. D., Jr; Bashford, D.; Bellott, M.; Dunbrack, R. L., Jr; Evanseck, J. D.; Field, M. J.; Fischer, S.; Gao, J.; Guo, H.; Ha, S. All-Atom Empirical Potential for Molecular Modeling and Dynamics Studies of Proteins. *J. Phys. Chem. B* **1998**, *102*, 3586−3616.
(105) Jorgensen, W. L.; Chandrasekhar, J.; Madura, J. D.; Impey, R. W.; Klein, M. L. Comparison of Simple Potential Functions for Simulating Liquid Water. *J. Chem. Phys.* **1983**, *79*, 926−935.
(106) Price, D. J.; Brooks, C. L., III A Modified TIP3P Water Potential for Simulation with Ewald Summation. *J. Chem. Phys.* **2004**, *121*, 10096−10103.
(107) Himo, F. Recent Trends in Quantum Chemical Modeling of Enzymatic Reactions. *J. Am. Chem. Soc.* **2017**, *139*, 6780−6786.
(108) Siegbahn, P. E. M.; Borowski, T. Modeling Enzymatic Reactions Involving Transition Metals. *Acc. Chem. Res.* **2006**, *39*, 729−738.
(109) Adamo, C.; Barone, V. Exchange Functionals with Improved Long-Range Behavior and Adiabatic Connection Methods without Adjustable Parameters: The mPW and mPW1PW Models. *J. Chem. Phys.* **1998**, *108*, 664−675.
(110) Petersson, G. A.; Bennett, A.; Tensfeldt, T. G.; Al-Laham, M. A.; Shirley, W. A.; Mantzaris, J. A Complete Basis Set Model Chemistry. I. the Total Energies of Closed-Shell Atoms and Hydrides of the First-Row Elements. *J. Chem. Phys.* **1988**, *89*, 2193−2218.
(111) Petersson, G. A.; Al-Laham, M. A. A Complete Basis Set Model Chemistry. II. Open-Shell Systems and the Total Energies of the First-Row Atoms. *J. Chem. Phys.* **1991**, *94*, 6081−6090.
(112) Hay, P. J.; Wadt, W. R. Ab Initio Effective Core Potentials for Molecular Calculations. Potentials for the Transition Metal Atoms Sc to Hg. *J. Chem. Phys.* **1985**, *82*, 270−283.
(113) Wadt, W. R.; Hay, P. J. Ab Initio Effective Core Potentials for Molecular Calculations. Potentials for Main Group Elements Na to Bi. *J. Chem. Phys.* **1985**, *82*, 284−298.
(114) Hay, P. J.; Wadt, W. R. Ab Initio Effective Core Potentials for Molecular Calculations. Potentials for K to Au including the Outermost Core Orbitals. *J. Chem. Phys.* **1985**, *82*, 299−310.
(115) Roy, L. E.; Hay, P. J.; Martin, R. L. Revised Basis Sets for the LANL Effective Core Potentials. *J. Chem. Theory Comput.* **2008**, *4*, 1029−1031.
(116) Grimme, S.; Ehrlich, S.; Goerigk, L. Effect of the Damping Function in Dispersion Corrected Density Functional Theory. *J. Comput. Chem.* **2011**, *32*, 1456−1465.
(117) Tomasi, J.; Mennucci, B.; Cammi, R. Quantum Mechanical Continuum Solvation Models. *Chem. Rev.* **2005**, *105*, 2999−3094.
(118) Cancès, E.; Mennucci, B.; Tomasi, J. A New Integral Equation Formalism for the Polarizable Continuum Model: Theoretical Background and Applications to Isotropic and Anisotropic Dielectrics. *J. Chem. Phys.* **1997**, *107*, 3032−3041.
(119) Becke, A. D. Density-Functional Thermochemistry. III. The Role of Exact Exchange. *J. Chem. Phys.* **1993**, *98*, 5648−5652.
(120) Zhao, Y.; Truhlar, D. G. The M06 Suite of Density Functionals for Main Group Thermochemistry, Thermochemical Kinetics, Noncovalent Interactions, Excited States, and Transition Elements: Two New Functionals and Systematic Testing of Four M06-Class Functionals and 12 Other Functionals. *Theor. Chem. Acc.* **2008**, *120*, 215−241.
(121) Grauffel, C.; Lim, C. Factors Governing When a Metal-Bound Water Is Deprotonated in Proteins. *Phys. Chem. Chem. Phys.* **2018**, *20*, 29625−29636.
(122) Kiefer, L. L.; Fierke, C. A. Functional Characterization of Human Carbonic Anhydrase II Variants with Altered Zinc Binding Sites. *Biochemistry* **1994**, *33*, 15233−15240.
(123) McCall, K. A.; Huang, C.-c.; Fierke, C. A. Function and Mechanism of Zinc Metalloenzymes. *J. Nutr.* **2000**, *130*, 1437S−1446S.
(124) Zastrow, M. L.; Pecoraro, V. L. Designing Hydrolytic Zinc Metalloenzymes. *Biochemistry* **2014**, *53*, 957−978.
(125) Zhu, X.; Barman, A.; Ozbil, M.; Zhang, T.; Li, S.; Prabhakar, R. Mechanism of Peptide Hydrolysis by Co-Catalytic Metal Centers Containing Leucine Aminopeptidase Enzyme: A DFT Approach. *J. Biol. Inorg. Chem.* **2012**, *17*, 209−22.

https://doi.org/10.1021/acs.jcim.2c00214
J. Chem. Inf. Model. 2022, 62, 2466−2480

(126) Chen, S. L.; Marino, T.; Fang, W. H.; Russo, N.; Himo, F. Peptide Hydrolysis by the Binuclear Zinc Enzyme Aminopeptidase from *Aeromonas proteolytica*: A Density Functional Theory Study. *J. Phys. Chem. B* **2008**, *112*, 2494−500.

https://doi.org/10.1021/acs.jcim.2c00214
J. Chem. Inf. Model. 2022, 62, 2466−2480